

# NEW H<sub>2</sub> JETS IN MONOCEROS R2

Klaus W. Hodapp<sup>1</sup>

## ABSTRACT

We are presenting a wide-field image of the Mon R2 star forming region obtained with WFCAM on UKIRT in the 2.12  $\mu\text{m}$  filter centered on the H<sub>2</sub> 1–0 S(1) emission line. We report the discovery of 15 new H<sub>2</sub> jets in Mon R2 and two in L 1646 and confirm most of these discoveries using archival Spitzer IRAC 4.5  $\mu\text{m}$  and 8.0  $\mu\text{m}$  images. We find that many of these protostellar jets are found in projection against the outflow cavities of the huge CO outflow in Mon R2, suggesting that the jets may be associated with an episode of star formation in Mon R2 triggered by this large, but now fossil, outflow. We also study the spatial distribution of small, localized reflection nebulae and find that these are distributed in the same way as photometrically identified Class I sources.

*Subject headings:* stars: pre-main-sequence — stars: formation — ISM: jets and outflows — ISM: Herbig-Haro objects

## 1. INTRODUCTION

The region studied here was first identified by van den Bergh (1966) as an association of optical reflection nebulae in their list of such objects and was labeled Monoceros R2, in short Mon R2. The Mon R2 molecular cloud complex extends over  $3^\circ \times 6^\circ$ , and the overall mass of this large molecular cloud has been estimated by Maddalena et al. (1986) to be  $9 \times 10^4 M_\odot$ . The Mon R2 molecular cloud contains several sites of star formation: GGD 11, GGD 12-15 (Gyulbudaghian, Glushkov, & Denisyuk 1978), L 1646 (Carpenter 2000), and the Mon R2 core, the main star formation site that is the subject of this study. The Mon R2 star forming region lies between the two optical reflection nebulae vdB 67 and vdB 69 (van den Bergh 1966) and has attracted considerable attention as a site of massive star formation, as a young embedded cluster, and as the source of one of the most powerful CO outflows known.

---

<sup>1</sup> Institute for Astronomy, University of Hawaii,  
640 N. Aohoku Place, Hilo, HI 96720,  
email: hodapp@ifa.hawaii.edu

Even though Mon R2 lies close to Orion in projection on the sky, its distance of  $830 \pm 50$  pc based on photometric parallaxes (Herbst & Racine 1976) is almost double that of the Trapezium cluster, e.g. (Stanke, McCaughrean, & Zinnecker 2002). Despite its larger distance, it is still close enough for detailed studies of the embedded young objects. The mass of molecular gas in the Mon R2 core has been determined by Ridge et al. (2003) using  $^{13}\text{CO}$  and  $\text{C}^{18}\text{O}$  maps. The rarer  $\text{C}^{18}\text{O}$  traces denser gas and resulted in a gas mass of  $1826 M_{\odot}$ , while the more abundant  $^{13}\text{CO}$  also samples the tenuous outer regions of the molecular core and gave a mass of  $2550 M_{\odot}$ . The molecular gas distribution is single-peaked with a slight indication of extended filaments to the south and south-west. To put this region into perspective, Mon R2 is smaller than the Orion Trapezium region in spatial extent, molecular mass, and number and total mass of embedded stars. It is, however, not far behind in many of these parameters.

Mon R2 has been noted as a source of a bipolar CO outflow by Loren (1981). This main Mon R2 molecular outflow was found by Wolf et al. (1990) to be one of the dynamically oldest ( $1.5 \times 10^5$  y), largest (7 pc), and most massive ( $100 M_{\odot}$ ) molecular outflows. Based on CO maps with higher spatial resolution than those of Wolf et al. (1990), Meyers-Rice & Lada (1991) argued that the Mon R2 CO outflow must consist of two bipolar outflows: one component seen almost head-on to explain the overlapping red and blue shifted velocity components seen in projection against the central cluster, and one component more inclined against the line of sight, to explain the bipolar outflow features. Both components could be modeled as paraboloidal shells with a linear velocity field that could result from velocity-sorting of clumpy outflow material. The detailed study of CO emission and multiple transitions of CS by Tafalla et al. (1997) showed that the massive outflow has created an hourglass-shaped cavity in the molecular cloud centered on the cluster of massive young stars. The cavity walls coincide with the limb-brightened shells of the blue-shifted outflow lobe. The axis of the paraboloidal outflow shell and cavity are oriented roughly at a position angle of  $-30^{\circ}$ .

The central group of luminous stars and the associated nebulosity were discovered in the near infrared by Beckwith et al. (1976). Much of the attention has been focused on the ring-like reflection nebula around IRS 1 discovered by Beckwith et al. (1976) and studied in more detail by Hodapp (1987), on the details of the cluster’s most luminous individual source (IRS 3) summarized in the most recent work by Preibisch et al. (2002), and on the distribution of molecular matter and the large outflow, summarized in Tafalla et al. (1997). In embedded young clusters like Mon R2, near-infrared (J, H, and K) photometry is a very useful tool for identifying young cluster members on the basis of their color excess over the reddened photospheres of old background stars. The first such study of Mon R2 was done by Carpenter et al. (1997). Most recently, the Initial Mass Function (IMF) in the Mon R2 cluster core was studied in detail by Andersen et al. (2006) on the basis of HST/NICMOS

data. They find that the ratio of the number of stars below solar mass to the number of objects in the brown dwarf mass range is similar to that found in the Trapezium cluster and in IC 348.

Compared to the widely used J, H, and K images used to characterize the stellar population of young clusters, the Spitzer IRAC images in four bands ranging from  $3.6\ \mu\text{m}$  to  $8.0\ \mu\text{m}$  allow the identification of younger and more deeply embedded objects. Further, they also allow the identification of objects with purely longer-wavelength infrared excess, indicating passive reprocessing disks, e. g. (Gutermuth 2005) and (Kumar et al. 2007). On the basis of near-infrared J, H, and K photometry, and of Spitzer mid-infrared photometry, Gutermuth (2005) found that Class I objects in Mon R2 are distributed in a filamentary pattern, while Class II objects are distributed more widely and evenly. However, even these IRAC bands are not sampling the youngest objects in a cluster completely, in particular those Class 0 and I objects that are oriented with their disks seen edge-on. Fortunately, those objects can still be found indirectly. The substantial accretion activity in the Class 0 and I phases of low-mass star formation is invariably associated with outflow activity, as was first noted by André, Ward-Thompson & Barsony (1993). These outflows easily break out of the dense molecular disk and the envelop enshrouding the young star, and are therefore readily detected in the near-infrared, due to the shock-excited emission at the interface between the outflow and the ambient molecular material, and in shocks within the outflow. The most easily accessible near-infrared shock-excited emission lines are the [FeII] line at  $1.644\ \mu\text{m}$  and the  $\text{H}_2$  1–0 S(1) line at  $2.122\ \mu\text{m}$ , the line studied here. Of these two emission lines, the  $\text{H}_2$  1–0 S(1) line traces lower excitation levels and is excited in virtually all deeply embedded jets propagating in molecular clouds. Therefore, shock-excited emission of molecular hydrogen is the earliest near-infrared signpost of outflow activity in a very young object and is usually observable long before the central star becomes observable in the near or mid infrared. Molecular hydrogen jets tend to have morphological features that are distinct from other forms of  $\text{H}_2$  emission in star forming regions, and are therefore easily recognized in imaging surveys.

Powerful jet activity is a byproduct of the short-lived main accretion phase of a forming star. When the accretion and jet activity fades after about  $10^5$  y, the envelope of molecular gas around a young star usually has formed two outflow cavities. When properly oriented, scattered light from these cavity walls gives the object the appearance of a bipolar nebula, or a cometary nebula if only one cavity can be seen. Objects of this morphology overlap with the Class I objects that can be identified photometrically using the Spitzer IRAC bands. Therefore, imaging surveys of star forming regions for protostellar jets and bipolar or cometary nebulae are a powerful tool for discovering very young (Class 0 or I) objects in or soon after their main accretion phase. Thanks to the recent availability of large-format

near-infrared cameras such surveys can now be conducted efficiently.

In this paper, we report the discovery of 17 extremely young objects in and around the Mon R2 star forming region by means of imaging their collimated outflows in the H<sub>2</sub> 1–0 S(1) emission line at 2.12  $\mu\text{m}$ . By comparison of the 2.12  $\mu\text{m}$  image and the Spitzer IRAC 4.5  $\mu\text{m}$  and 8.0  $\mu\text{m}$  images we discuss the most plausible identification of the source of each outflow. The large number of outflows indicates that star formation is active all through the Mon R2 molecular cloud. We will discuss the spatial distribution of the newly discovered extremely young stars in relation to the large, old molecular outflow in Mon R2.

## 2. OBSERVATIONS AND DATA REDUCTION

### 2.1. UKIRT WFCAM 2.12 $\mu\text{m}$ Imaging

The purpose of this project was not the detailed study of any particular jet, but rather the discovery of new objects in the Mon R2 star forming region that indicate the presence of stars in their youngest phase of evolution. Also, completeness in the discovery of H<sub>2</sub> outflows was not a realistic goal for this survey of a region with such extensive reflection nebulosity and, most likely, also fluorescently excited H<sub>2</sub> emission (e. g., Black & Dalgarno (1976)) that both tend to confuse any search for H<sub>2</sub> outflows. Therefore, in the interest of maximizing the scientific return of the observing time used, we did not obtain an image at a continuum wavelength adjacent to the S(1) line, or in a broad K-band filter to distinguish between emission line features and continuum reflection nebulosity. As discussed below, the identification of H<sub>2</sub> jets relied on morphological arguments and confirmation, if possible, by archival Spitzer IRAC images.

Wide-field near-infrared images of the Mon R2 region were obtained in the night of October 20, 2005, UT, at the United Kingdom Infrared Telescope (UKIRT). The Wide-Field Camera (WFCAM) (Casali et al. 2007) was used with a filter centered at 2.121  $\mu\text{m}$  with  $\Delta\lambda = 0.021 \mu\text{m}$  that includes the H<sub>2</sub> 1–0 S(1) line. The field was roughly centered on the well-studied Mon R2 cluster of infrared sources. The WFCAM uses four Teledyne (formerly Rockwell) HAWAII-2 2048×2048 HgCdTe infrared detector arrays at a pixel scale of 0.4'' pixel<sup>−1</sup>, arranged in the camera focal plane with a spacing of 0.94 of the detector size between the devices. To achieve full coverage of a 0.75 square degrees region of the sky, four telescope pointings are required, which in WFCAM terminology are called a “tile”. At each tile position, a five-point dither pattern (3.2'' spacing) is used to avoid bad pixels and other detector array artifacts. Finally, at each dither position, a four-point micro-step pattern with a half-pixel (0.2'') step size is used to oversample the image. For our observations, an

on-chip exposure time of 40 s was chosen, and the detectors were read out in non-destructive mode, sampling the accumulating signal 41 times during the integration time. The readnoise achieved in this mode of operation is  $\approx 20 \text{ e}^- \text{ rms}$ . The on-sky integration time was 800 s, except in the overlap regions of the tile. With a distance to Mon R2 of 830 pc, one arcminute in our images corresponds to a projected distance of 0.24 pc.

The data were processed by the Cambridge Astronomical Survey Unit (CASU) using the procedures described by Dye et al. (2006). Astrometric calibration relative to the 2MASS catalog (Skrutskie et al. 2006) was performed and a plate solution was written into the file headers. All coordinates in this paper therefore are given in J2000.0 and are indirectly based on the 2MASS coordinate system. After retrieval of the reduced data from the WFCAM Science Archive the final assembly of the full tile image was done with IRAF scripts that used the image header information to assemble the individual images into a tangential projection image of the full tile.

The central region of the resulting image is shown in Fig. 1. The image shows the well-known Mon R2 cluster near the center, and the two reflection nebulae to the west (vdB 67) and east (vdB 69) of it. Filamentary emission extends mostly to the north and east of the main star forming region. The lowest contours of the blue and red shifted CO maps of Wolf et al. (1990) are superposed on Fig. 1. There is no large-scale feature visible that would be morphologically associated with the main CO outflow centered on IRS 2 (identified in Fig. 2) that has a rather poorly defined outflow axis at P.A.  $\approx -45^\circ$  (Wolf et al. 1990) or with the outflow cavity whose axis is oriented at  $\approx -30^\circ$  (Tafalla et al. 1997) and (Choi et al. 2000).

## 2.2. Archival Spitzer Images

The IRAC camera is the main near and mid-infrared imaging instrument of the Spitzer cryogenically cooled space telescope (Fazio et al. 2004). All the four IRAC channels contain emission lines of  $\text{H}_2$ . Of the four IRAC channels, band 2 centered at  $4.5 \mu\text{m}$  is particularly well suited to detect  $\text{H}_2$  emission. From a discussion of different shock models, Smith & Rosen (2005) concluded that shock-excited  $\text{H}_2$  emission in the  $4.5 \mu\text{m}$  band is an order of magnitude brighter than in the other channels for a wide range of shock conditions. The IRAC band 2 ( $4.5 \mu\text{m}$ ) contains the  $\text{H}_2$  0-0 S(9) line at  $4.694 \mu\text{m}$  and emission in this line shows morphological features closely identical to those seen in  $\text{H}_2$  1-0 S(1) at  $2.122 \mu\text{m}$ , but is less affected by dust extinction. Therefore, despite the fact that the broad IRAC band 2 also contains other important molecular features such as CO ( $\nu=1-0$  at  $4.45 - 4.95 \mu\text{m}$ ) and the atomic Hydrogen Br $\alpha$  line at  $4.052 \mu\text{m}$ , images in this band often show very similar jet morphology

to  $2.12\ \mu\text{m}$  S(1) images (Smith et al. 2006). By contrast, Smith & Rosen (2005) find that IRAC band 1 ( $3.6\ \mu\text{m}$ ) is dominated by vibrationally excited lines with higher excitation energy than the 1–0 S(1) line, so that shock features appear sharper in band 1 than in a  $2.12\ \mu\text{m}$  1–0 S(1) image. The Spitzer  $3.6\ \mu\text{m}$ ,  $5.8\ \mu\text{m}$ , and  $8.0\ \mu\text{m}$  bands also contain bright PAH emission at  $3.3\ \mu\text{m}$ ,  $6.2\ \mu\text{m}$ , and  $7.7\ \mu\text{m}$ , respectively. In a region like Mon R2, this strong and often filamentary emission tends to mask shock-excited emission from jets.

Spitzer IRAC images were downloaded from the Spitzer archive. The data used here were originally obtained for a program by G. Fazio. Partial results of their study of the distribution of stars based on JHK and Spitzer/IRAC colors have been presented by Gutermuth (2005).

The available archival Spitzer data do not cover the whole field of our WFCAM observations, so that we do not have the corresponding longer-wavelength data for all of the outflows discovered here. For those objects where all Spitzer bands are available, we discuss the  $4.5\ \mu\text{m}$  and  $8.0\ \mu\text{m}$  data. The  $4.5\ \mu\text{m}$  data usually show the outflows, but at relatively low signal-to-noise ratio and with poorer spatial resolution than the UKIRT data. The  $8.0\ \mu\text{m}$  data do not usually show the outflow itself, but in many cases show the molecular clump around the driving source either in thermal dust emission or in some cases in absorption against PAH background emission. The  $8.0\ \mu\text{m}$  images therefore primarily serve to confirm the identification of the driving source. In some cases the band 2 ( $4.5\ \mu\text{m}$ ) data were not available and for one object band 1 data ( $3.6\ \mu\text{m}$ ) data are shown instead for the purpose of source confirmation.

### 2.3. Criteria for Identifying H<sub>2</sub> Jets

This simple imaging project was motivated by the success of similar observations in identifying H<sub>2</sub> jets, e. g. the early survey of NGC 1333 by Hodapp & Ladd (1995), the extensive survey of Orion A by Stanke, McCaughrean, & Zinnecker (2002), the survey of the distant massive star forming region W 51 by Hodapp & Davis (2002), and the recent work on DR21/W75 by Davis et al. (2007). Well over one hundred of these collimated H<sub>2</sub> jets have now been imaged and their morphology is quite unique and well recognizable. Empirically, shock excited H<sub>2</sub> emission can, in most cases, be distinguished from fluorescently excited H<sub>2</sub> emission on the basis of morphological arguments. The physical basis for this is that the cooling time of shock-excited molecular hydrogen is typically only a few years (Shull & Hollenback 1978), during which time shock fronts travel only a fraction of an arc-second in typical star forming regions. Shock-excited emission therefore usually appears as small but resolved knots, filaments, and bow shocks. In contrast, fluorescently excited

molecular hydrogen emission varies on the scale of typical density inhomogeneities in molecular clouds and therefore tends to be much more smoothly distributed. The same is true for large-scale continuum reflection nebulosity.

Our criteria for identifying  $\text{H}_2$  jets in Mon R2 therefore were that they must consist of a string of resolved  $\text{H}_2$  emission knots. If a bow shock is found at the end of a string of emission knots, this is regarded as additional and convincing evidence for the existence of a jet. In cases where both sides (lobes) of a jet are visible, a high degree of central symmetry in the distribution of emission knots serves as supporting evidence for the identification of a jet. Sometimes, but not always, faint filamentary emission arising from the outflow cavity walls connects the individual emission knots. If such filamentary emission is seen, it serves as additional evidence supporting the identification of a jet. The  $\text{H}_2$  jets identified by these criteria are listed in Table 1, and identified in Fig. 1 as large circles.

Finally, many young stars show reflection nebulae of bipolar or cometary morphology or nebulae otherwise clearly associated with individual stars, properties that we summarize by the term "localized". In addition to their characteristic morphology, they show a more pronounced drop in surface brightness away from the illuminating central star than the shock emission knots in  $\text{H}_2$  jets. In Table 2, we list such localized nebulae that were found on our  $2.12\mu\text{m}$  image on Mon R2, but were not classified as likely  $\text{H}_2$  jets. Nebulous features that are simply knots in the large-scale nebulosity permeating the center of the Mon R2 cluster are not listed in Table 2. Similar to the situation with the  $\text{H}_2$  jets, this list cannot be expected to be complete, due to sensitivity limits, high extinction in some parts of the molecular cloud, and confusion with the large-scale reflection nebulosity and filamentary emission present in the Mon R2 region. The localized reflection nebulae are indicated as small squares in Figs. 1 and 2.

The K' survey of known CO outflow sources by Hodapp (1994) showed that many of these outflow sources are associated with such localized reflection nebulae. Reflection nebulae, in particular of bipolar or cometary morphology, are produced by light scattered from the inside walls of the cavity produced by an outflow in the molecular material surrounding a young star. While the association of reflection nebulae with young age of an individual star and with outflow activity is less direct than for  $\text{H}_2$  jets, the presence of large numbers of these localized reflection nebulae nevertheless indicates a population of very young stars, probably stars just after their main accretion and outflow phase.

### 3. RESULTS AND DISCUSSION

#### 3.1. The Environment of the Mon R2 Cluster

Fig. 1 shows an extended system of emission filaments to the north and east of the cluster, besides the known reflection nebulae vdB 67 and 69, the nebulosity associated with the Mon R2 cluster, and the individual H<sub>2</sub> jets reported here.

These filaments coincide with the optical reflection nebula vdB 68, and are also strongly visible in all Spitzer IRAC bands, probably indicating a combination of H<sub>2</sub> and PAH emission fluorescently excited by the illuminating star of vdB 68, a B2V star (Herbst & Racine 1976). The filaments seen in Fig. 1 are oriented at a position angle of  $\approx 35^\circ$ , similar to some of the filamentary structure seen in the optical reflection nebula. It should be noted that this orientation of the filaments is similar to the polarization angle of background star polarization in the region of vdB 68 as measured by Jarrett et al. (1994) in the R band, which indicates the projected direction of the local magnetic field.

On the Digital Sky Survey (DSS) blue and red images, an extensive system of filaments is seen in absorption against the background reflection nebulosity in the area south and east of vdB 67, the Mon R2 cluster, and vdB 69. These filaments are also oriented along the direction of the local magnetic field, as measured by the R-band polarimetry of Jarrett et al. (1994). Our 2.12  $\mu\text{m}$  S(1) image does not show any emission from these filaments located in the south east of the embedded cluster.

From the fact that these systems of filaments are readily visible at optical wavelengths, we conclude that they lie on the front side of the Mon R2 molecular core. Since the polarization vectors of more deeply embedded sources in and near the Mon R2 cluster (Hodapp 1987) follow the pattern of the magnetic field measured to the south and west of the cluster, and since the cluster is located at the intersection of the two patterns of magnetic field direction, it can be speculated that the formation of the Mon R2 cluster was triggered by a collision to two molecular clouds, as discussed by Jarrett et al. (1994).

The core of the Mon R2 cluster and the bright reflection nebulosity permeating it are shown in more detail in Fig. 2. From polarization measurements of this ring-like infrared reflection nebulosity near the core of the Mon R2 cluster by Hodapp (1987), it is clear that IRS 2 is its dominant source of illumination. The brighter source IRS 3 does not significantly contribute to the illumination (as measured by polarization) of the ring-like nebula, and therefore must be located either in front or behind the nebula and the core of the Mon R2 cluster. Some elongated emission features are seen east of IRS 3 and lie in a direction similar to the filaments observed near vdB 69. This would suggest that IRS 3 is illuminating some



of these filaments and that it lies in front of the rest of the Mon R2 cluster.

### 3.2. Previously Known Outflows

The overwhelming size and total mass of the main Mon R2 CO outflow (Loren 1981) makes it difficult to find evidence for other outflows in the velocity field measured in  $^{12}\text{CO}(2-1)$  or  $^{13}\text{CO}(2-1)$ . It should be noted that Meyers-Rice & Lada (1991) have argued that the distribution of high velocity CO gas in this main outflow can only be explained by a superposition of two independent outflows with different orientations, one almost head-on and the other more inclined to produce the bipolar appearance. Despite the overwhelming emission from these two main outflows, two additional possible outflows associated with the Mon R2 cluster have been discovered by CO emission line mapping by Tafalla et al. (1997) and a third possible outflow (a microjet from IRS 3) was found by Preibisch et al. (2002).

The  $^{12}\text{CO}(2-1)$  and  $^{13}\text{CO}(2-1)$  velocity channel maps of Tafalla et al. (1997) (their Figs. 3 and 4) show a redshifted high velocity component (Mon R2-N) about  $80''$  to the north of the central cluster, coinciding with “Object 1” of Cohen & Frogel (1977). This object is the brightest of a group of embedded stars north of the ring-like reflection nebula, and is itself embedded in reflection nebulosity with a complex filamentary structure shown in Fig. 2. The brightest star in this sub-group of the Mon R2 cluster is located at  $6^{\text{h}}7^{\text{m}}45^{\text{s}}.9$ ,  $-6^{\circ}21'47''$ . Also, Tafalla et al. (1997) discuss a strongly blueshifted  $^{12}\text{CO}$  feature ( $-100'', -40''$ ) from IRS 1 that also coincides with an enhancement of CS emission, indicating the presence of a deeply embedded object. We refer to this object by the initials of the authors as “TBWW97 CO-100,-40”. At its position ( $6^{\text{h}}7^{\text{m}}39^{\text{s}}.2$ ,  $-6^{\circ}23'44''$ ), we note a faint, slightly elongated infrared object on the S(1) image, surrounded by several small patches of nebulosity (Fig. 2 and Fig. 3, upper panels).

The Spitzer  $4.5\ \mu\text{m}$  image shows the same object morphology and confirms that the marginally extended  $2.12\ \mu\text{m}$  object is not an embedded star. The Spitzer  $8.0\ \mu\text{m}$  image shows extended emission in this region. The high-velocity CO gas and the shock-excited  $\text{H}_2$  emission indicate a spatially compact outflow, without a clear jet morphology. This object is shown near the western edge of Fig. 2 (labeled “CO”). and in the first panel of Fig. 3.

The infrared source IRS 3 was noted by (Beckwith et al. 1976) to be extended and was later resolved into a number of sources. The highest spatial resolution image are the speckle interferometry results by Preibisch et al. (2002) that list point sources IRS 3 A - F, of which A, B, and C are associated with strong reflection nebulosity, and B is possibly associated with a microjet of about  $0.5''$  length. The detailed CO velocity maps by Giannakopoulou et al.

(1997) show that IRS 3 is not associated with the big Mon R2 CO outflow, but that it is a separate source of very high-velocity CO outflow, even though a clear bipolar feature was not detected.

### 3.3. The Spatial Distribution of H<sub>2</sub> Jets

The newly discovered H<sub>2</sub> jets are overlayed on Fig. 1 as open circles with labels. Also overlayed are the lowest contours of the blue and redshifted features in the CO map of Wolf et al. (1990). Their map was chosen over the higher spatial resolution maps of Meyers-Rice & Lada (1991) and Tafalla et al. (1997) since it covers a larger area with higher sensitivity to faint extended features. The only sites of star formation lying clearly outside of the CO outflow lobes are the newly discovered HOD07 1 to the west of the main cluster, and the previously known young object GGD 11. The longest of the newly discovered H<sub>2</sub> jets (HOD07 13) lies just south of the redshifted CO lobe.

The CO outflows probably have a shell structure with a relatively empty cavity near the outflow axis (Meyers-Rice & Lada 1991). Since the outflowing material interacts turbulently with the molecular material of the ambient cloud, triggered star formation would be expected near the interface between the shell and the ambient cloud. In projection, the highest density of triggered star formation sites would be expected where we look tangentially along the shell wall, and a smaller number where we look onto the front and back sides of the outflow shells. The overall distribution of newly found H<sub>2</sub> jets outside of the central cluster roughly matches this expectation. Note in particular that the small cluster associated with HH 866 is projected against the tip of the blueshifted CO contour of Wolf et al. (1990), and that the group of H<sub>2</sub> jets HOD07 2, 3, 6, 8, and 9 lie close to the eastern edge of the blueshifted CO contour, and behind two secondary blue-shifted CO emission maxima. These spatial coincidences strongly suggest that sites of recent star formation outside the main Mon R2 cluster may have been triggered by turbulent interaction of the massive main Mon R2 outflow with the ambient molecular material.

In the following, we discuss the newly discovered H<sub>2</sub> jets individually on the basis of their morphology and, when available, by a comparison of the near-infrared 2.12  $\mu$ m S(1) image to longer wavelength Spitzer images. The objects are numbered in the sequence of increasing R.A., and labeled by the prefix HOD07. All coordinates are given in the J2000.0 system. To allow an easy comparison of their sizes, the overview 2.12  $\mu$ m images based on the UKIRT/WFCAM data are all shown on the same spatial scale. Similarly, the detailed views in the figures comparing WFCAM and Spitzer/IRAC results are all on the same, but finer, spatial scale, with the exception of Fig. 6, where this was not practical.

The small localized reflection nebulae that we found on our 2.12  $\mu\text{m}$  image, but did not classify as jets, are listed in Table 2 and are indicated by small squares in Figs. 1 and 2. These localized reflection nebulae are concentrated to the south of the Mon R2 cluster, closer to the cluster than the  $\text{H}_2$  jets found to the south and south west of the cluster. Since the reflection nebulae represent a more advanced state of star formation than the jets, this distribution might indicate a sequence of triggered star formation to the south of the main Mon R2 cluster, in the region where the blue and red shifted CO contours overlap.

### 3.4. Discussion of Individual $\text{H}_2$ Jets

#### 3.4.1. HOD07 1

The  $\text{H}_2$  jet HOD07 1 has a very symmetric bipolar appearance, as is shown in Fig. 4. We note a high degree of similarity in the shape and relative intensity of corresponding knots in the two lobes of the jet. We interpret the two extended patches of nebulosity  $\approx 3''$  east (labeled 1E) and west (labeled 1W) of the apparent center of symmetry at coordinates  $6^{\text{h}}7^{\text{m}}10^{\text{s}} -6^{\circ}26'34''$  (marked by a circle in Fig. 4) as emission or scattered light from the two outflow cavities, and assume that the driving source is hidden from direct view and located near that position in the dark region between those two emission knots. From this position, the eastern jet lobe has a position angle of  $\approx 60^\circ$ . Since HOD07 1 is not included in the publicly released Spitzer images of the Mon R2 region, this position of the central source could not be confirmed by longer wavelength data.

Going symmetrically outwards from the assumed position of the driving source, there is a pair of faint emission knots at  $6^{\text{h}}7^{\text{m}}9^{\text{s}}.5, -6^{\circ}26'44''$  (2W) and  $6^{\text{h}}7^{\text{m}}11^{\text{s}}.6, -6^{\circ}26'22''$  (2E), respectively. The next pair of relatively faint emission knots is at  $6^{\text{h}}7^{\text{m}}9^{\text{s}}.0, -6^{\circ}26'46''$  (3W) and  $6^{\text{h}}7^{\text{m}}12^{\text{s}}.4, -6^{\circ}26'16''$  (3E). Further away from the central source we find two complex systems of bright emission knots, containing two (west) and three (east) individual knots, centered at  $6^{\text{h}}7^{\text{m}}8^{\text{s}}.2, -6^{\circ}26'52''$  (4W) and  $6^{\text{h}}7^{\text{m}}12.9, -6^{\circ}26'11''$  (4E), respectively. Both of these emission regions show a bend of  $\approx 45^\circ$  to the left in the direction of motion. To the west of the central source, at  $6^{\text{h}}7^{\text{m}}7^{\text{s}}.5, -6^{\circ}26'54''$  (5W) there is one additional very strong emission knot of approximately triangular shape with no detectable counterpart in the east. Finally, the most distant, approximately symmetric set of faint shock emission features is located at  $6^{\text{h}}7^{\text{m}}6^{\text{s}}.3, -6^{\circ}26'57''$  (6W) and  $6^{\text{h}}7^{\text{m}}16^{\text{s}}.7, -6^{\circ}25'53''$  (6E). On the eastern side, this faint extended nebulosity coincides with the images of several stars, but there is no evidence to suggest that these stars are physically associated with the outflow.

It is noteworthy that the bend in the otherwise straight bipolar jet coincides with the

strongest emission knots. Bent or S-shaped jets as a result of disk precession in a binary system were discussed by Terquem et al. (1999) and Bate et al. (2000). We speculate that the main accretion and outflow event that produced these strong systems of emission knots was triggered by a close stellar encounter, most likely with a binary star component on an elliptical orbit, and that this encounter was also responsible for a change in the disk orientation and therefore the jet direction.

### 3.4.2. HOD07 2

The extended S(1) emission with shock-like morphology labeled HOD07 2 in Fig. 5 at  $6^h7^m30^s.5$ ,  $-6^\circ11'51''$  consists of two distinct knots of emission, suggesting that this is a short jet (P.A.  $\approx 120^\circ$ ) originating from a star that itself is too obscured to be directly visible. The position of the more compact shock emission knot is the position given above and in Table 1. The Spitzer  $8\ \mu\text{m}$  image (Fig. 6, bottom panel) shows extended emission centered on a point source at  $6^h7^m30^s.9$ ,  $-6^\circ11'48''$ . While this point source indicates other ongoing star formation activity in this region, its position does not coincide with the jet HOD07 2 and it therefore cannot be identified with the driving source of this jet.

### 3.4.3. HOD07 3

The bow shock HOD07 3 (Fig. 5) at  $6^h7^m31^s.6$ ,  $-6^\circ12'47''$  is probably driven by a source some distance away to the south east of the shock. Projecting back from the bow shock in this direction (P.A.  $\approx 147^\circ$ ) we find a string of faint, slightly extended knots of  $2.12\ \mu\text{m}$  emission. These faint emission features, indicated by arrows in Fig. 5, are located at  $6^h7^m33^s.2$ ,  $-6^\circ13'03''$ , at  $6^h7^m34^s.1$ ,  $-6^\circ13'24''$ , and at  $6^h7^m39^s.3$ ,  $-6^\circ14'01''$ . Overall, they appear to form a jet with multiple, faint internal shocks, ending in the bright bow shock. All these emission knots are confirmed by the Spitzer  $4.5\ \mu\text{m}$  data, even though only the knot closest to the bow shock is included in Fig. 6, where we show the bow shock at  $2.12\ \mu\text{m}$ ,  $4.5\ \mu\text{m}$ , and  $8.0\ \mu\text{m}$ . However, the position of the driving source of this jet could not be identified, neither on the WFCAM image nor the Spitzer images. We speculate that the jet emerges from deep within the molecular cloud and that only the terminating bow shock moving towards the observer is seen at relatively low extinction. Therefore, as indicated in Fig. 5, the position listed for this jet in Table 1 is that of the bow shock.

#### 3.4.4. *HOD07 4*

Two knots of  $\text{H}_2$  emission are visible to the west of the star at  $6^{\text{h}}7^{\text{m}}35^{\text{s}}.3$ ,  $-6^{\circ}20'00''$  in Fig. 7 and the top panel of Fig. 8. However, the extended nebulosity associated with the south-western of these knots is not connected with this star, strongly suggesting that this star may not be physically associated with the  $\text{H}_2$  emission. A second, fainter system of  $\text{H}_2$  emission with a bow shock morphology is visible at  $6^{\text{h}}7^{\text{m}}35^{\text{s}}.9$ ,  $-6^{\circ}19'56''$ , to the east-northeast of this star. The IRAC  $3.6\ \mu\text{m}$  (not shown here) and  $4.5\ \mu\text{m}$  images (Fig. 8, top center) show faint curved nebulosity connecting the  $2.12\ \mu\text{m}$  features with a very faint star at position  $6^{\text{h}}7^{\text{m}}37^{\text{s}}.6$ ,  $-6^{\circ}19'54''$  that is visible on the  $2.12\ \mu\text{m}$  UKIRT image as well as on the two shorter wavelength IRAC images. There is no evidence for a counterjet, bent or straight, emerging from the position of that faint star. Unfortunately, the longer wavelength IRAC archival images at this position are not of useable quality. From the available data we conclude that the S(1) shock emission and the S-shaped feature in the IRAC  $3.6\ \mu\text{m}$  and  $4.5\ \mu\text{m}$  images represent the less obscured parts of a jet emerging from the star at  $6^{\text{h}}7^{\text{m}}37^{\text{s}}.6$ ,  $-6^{\circ}19'54''$ . To explain the bending of the jet, it must be emitted from a precessing disk, similar to the case of IRAS 03256+3055 in NGC 1333 discussed by Hodapp et al. (2005).

#### 3.4.5. *HOD07 5*

The position given here for HOD07 5:  $6^{\text{h}}7^{\text{m}}38^{\text{s}}.7$ ,  $-6^{\circ}21'14''$ , indicated by a circle in Fig. 7 and Fig. 8, middle panel, is that of a faint extended emission feature near the apparent symmetry center of a system of shocks oriented at a position angle of  $\approx 32^{\circ}$ . This central object is visible on the UKIRT  $2.12\ \mu\text{m}$  image, but is much brighter on the Spitzer  $4.5\ \mu\text{m}$  image, indicating heavy obscuration. Also, the  $2.12\ \mu\text{m}$  image of this central feature shows a marginally detected bifurcation, indicating a disk seen in absorption against the extended emission or a disk shadow. We tentatively conclude that the driving source is not directly visible at near-infrared wavelengths, but that emission and/or scattered light very close to the source has been detected, and that the collimating disk is seen nearly edge-on. From this driving source, the jet extends along a position angle of  $\approx 30^{\circ}$ . The closest pair of shock emission knots is about  $5''$  to the north and south of the driving source. A second pair of emission features  $\approx 20''$  to the north and south appears less symmetric, with the southern shock extending further away from the source.

### 3.4.6. *HOD07 6*

To the west of the center of Fig. 9 and in Fig. 10 (top panels), a faint string of four  $2.12\ \mu\text{m}$  S(1) emission knots (labeled 6) and one larger emission knot further to the south west at  $6^{\text{h}}7^{\text{m}}38^{\text{s}}.7\ -6^{\circ}11'59''$  are all roughly aligned at P.A.  $\approx 45^{\circ}$ . The position of the central source cannot be determined with any certainty, and the Spitzer images do not provide additional information in this case. For lack of any better information, we list this jet by the coordinate of the approximate center of symmetry of the four northernmost emission knots located at  $6^{\text{h}}7^{\text{m}}41^{\text{s}}.2, -6^{\circ}11'14''$ , implicitly assuming this as a plausible position of a central source if these knots are, as in many other cases, symmetric shock fronts in a bipolar jet.

### 3.4.7. *HOD07 7*

The position given for this object in Table 1 is that of a faint star at  $6^{\text{h}}7^{\text{m}}41^{\text{s}}.5, -6^{\circ}21'28''$  roughly between two bright knots of S(1) emission in Fig. 7 and Fig. 8 (bottom panels) that define a jet axis along P.A.  $\approx 30^{\circ}$ . Faint filamentary emission extends back from the shocks to the immediate vicinity of this star, strongly suggesting that it is the source of the jet. On the  $2.12\ \mu\text{m}$  image, the northern jet bends to the east and the southern jet to the west about  $8'' - 10''$  from the star, suggesting a strongly precessing jet. The two brightest S(1) emission knots are located near the bend in the jet (in the north) and slightly beyond it in the south. This jet morphology can be understood by assuming that the bent, contiguous jet was formed by a precessing driving source. The two emission knots lying outside of the contiguous jets could be the product of a single burst of higher outflow velocity. The fact that these higher velocity knots were emitted in the same projected direction as the strongest bend in the jet may indicate that the strong precession of the driving source's accretion disk that caused this bend may also have caused the higher accretion rate that in turn produced the higher outflow intensity and velocity found in the two brighter knots.

The IRAC  $3.6\ \mu\text{m}$  (not shown here) and  $4.5\ \mu\text{m}$  (Fig. 8, bottom center) images show the strongest, and spatially extended emission associated with the northern of the two S(1) emission regions. To the east of this object, extended emission is seen both on the S(1) image and on the IRAC  $4.5\ \mu\text{m}$  and  $8.0\ \mu\text{m}$  images, and this emission appears to be associated with a filament extending from the Mon R2 central cluster. Whether this filament is physically close to the driving source of the outflow or whether the outflow interacts with the filament cannot be conclusively determined. However, the different emission flux levels in the northern and southern lobe could be understood if the northern jet ran into denser material.

### 3.4.8. *HOD07 8*

On the  $2.12\ \mu\text{m}$  image in Fig. 9, this jet extends from an unresolved object at  $6^{\text{h}}7^{\text{m}}43^{\text{s}}.7$ ,  $-6^{\circ}10'46''$  to a knot at  $6^{\text{h}}7^{\text{m}}44^{\text{s}}.4$ ,  $-6^{\circ}10'11''$ , a position angle of  $16^{\circ}$  and distance of  $36''$ , corresponding to a projected length of  $0.14\ \text{pc}$ . The jet axis is outlined by extended  $2.12\ \mu\text{m}$  emission. The only bright  $8.0\ \mu\text{m}$  object (Fig. 10) associated with this jet is the southern emission knot. It is therefore likely that this  $8.0\ \mu\text{m}$  object is the central star driving a jet where predominantly only one side is visible. The position of this bright mid-infrared source is listed as the position of the jet in Table 1 and shown in Fig. 9 and Fig. 10. On the  $2.12\ \mu\text{m}$  image, emission extends about  $2.5''$  to the south of the unresolved central source, suggesting that this is part of the jet's southern lobe.

### 3.4.9. *HOD07 9*

In Fig. 9, a well developed bow shock is located to the west of a star at  $6^{\text{h}}7^{\text{m}}44^{\text{s}}.0$ ,  $-6^{\circ}11'2''$ . An emission feature behind the bow shock, near the center of the arc formed by the bow, could be a Mach disk associated with the bow shock. The driving source of this bow shock cannot be determined with certainty from the data available to us. We are discussing two possible identifications for the driving source: The most plausible candidate for the driving source of this bow shock is the star at  $6^{\text{h}}7^{\text{m}}44^{\text{s}}.0$ ,  $-6^{\circ}11'02''$  that is the second brightest  $4.5\ \mu\text{m}$  and  $8.0\ \mu\text{m}$  source in Fig. 10 and that shows extended emission on the S(1) image indicating an illuminated outflow cavity, opening towards the west. We use this position at  $6^{\text{h}}7^{\text{m}}44^{\text{s}}.0$ ,  $-6^{\circ}11'2''$  as the nominal position of this jet in Table 1.

A much fainter, slightly extended object is visible on the UKIRT S(1) image at  $6^{\text{h}}7^{\text{m}}43^{\text{s}}.6$ ,  $-6^{\circ}10'58''$  and is also detectable, partly blended with the object described just above, on the Spitzer  $4.5\ \mu\text{m}$  image. The only reason to consider this object as an alternative candidate for the driving source of the bow shock is that it is more precisely located on the symmetry axis of the bow shock. This object, on the other hand, is also located on the axis of the jet source HOD07 8, and may just be another shock front of the southern part of that jet. The brightest source in Fig. 10 at any of the wavelengths discussed here is a cometary reflection nebula at  $6^{\text{h}}7^{\text{m}}43^{\text{s}}.4$ ,  $-6^{\circ}11'16''$  that we list as reflection nebula R5 in Table 2.

### 3.4.10. *HOD07 10*

Just west of its center Fig. 2 shows  $2.12\ \mu\text{m}$  S(1) emission with the morphology of a jet ending in a bow shock at  $6^{\text{h}}7^{\text{m}}43^{\text{s}}.0$ ,  $-6^{\circ}24'20''$ . This object is also shown in the bottom panels

of Fig. 3. The bow shock is strongly detected in the Spitzer IRAC 4.5  $\mu\text{m}$  image and is also indicated in the 8.0  $\mu\text{m}$  image. It is not clear where the driving source for this jet is located. The jet can be traced to an extended feature located at  $6^{\text{h}}7^{\text{m}}44^{\text{s}}.1$ ,  $-6^{\circ}23'59''$  and detected in both the 2.12  $\mu\text{m}$  and IRAC 4.5  $\mu\text{m}$  images. It is embedded in the emission surrounding the central Mon R2 cluster. This may be just another knot in a jet emerging from deeply inside the molecular cloud, or this may indicate the position of the driving source. There is no enhanced flux in the 8.0  $\mu\text{m}$  image at that position. Nevertheless, we adopt the position of this putative driving source as the formal coordinates of this jet called HOD07 10. A second shock front, located at  $6^{\text{h}}7^{\text{m}}43^{\text{s}}.6$ ,  $-6^{\circ}24'11''$  appears as the brightest of a series of internal shocks along the jet axis, which is oriented at a position angle of  $\approx 220^{\circ}$ .

#### 3.4.11. HOD07 11

The region shown in Fig. 11 contains 2 separate systems of  $\text{H}_2$  knots shown in more detail in Fig. 12. A well-defined bow shock located at  $6^{\text{h}}7^{\text{m}}48^{\text{s}}.6$ ,  $-6^{\circ}19'03''$  and several fainter knots of 2.12  $\mu\text{m}$  S(1) emission south-west from it suggest a jet with an axis oriented at P.A.  $\approx 23^{\circ}$ . The last S(1) emission knot at  $6^{\text{h}}7^{\text{m}}46^{\text{s}}.9$ ,  $-6^{\circ}20'6''$  coincides with a faint Spitzer 4.5  $\mu\text{m}$  object (Fig. 12, center panel), but is most likely just the 4.5  $\mu\text{m}$  emission of the same emission knot, and not the driving source itself. The Spitzer 4.5  $\mu\text{m}$  and 8.0  $\mu\text{m}$  images in Fig. 12 show a stronger mid-infrared source at approx.  $6^{\text{h}}7^{\text{m}}46^{\text{s}}.8$ ,  $-6^{\circ}20'12''$  just south-west of the position of the last observed S(1) knot in this string. This object is not detected in our near-infrared S(1) image and therefore must be very deeply embedded. We tentatively identify this mid-infrared source as the driving source of the jet HOD07 11.

#### 3.4.12. HOD07 12

The object at  $6^{\text{h}}7^{\text{m}}49^{\text{s}}.8$ ,  $-6^{\circ}20'43''$  in Fig. 11, HOD07 12, has the morphology of a faint bipolar nebula seen nearly edge-on, suggesting that it could be the source of a jet. The Spitzer 4.5  $\mu\text{m}$  image in Fig. 12 shows this object as an unresolved source, while the 8.0  $\mu\text{m}$  image does not show the object. Two other knots of S(1) emission lie to the south-east at  $6^{\text{h}}7^{\text{m}}51^{\text{s}}.6$ ,  $-6^{\circ}20'58''$  and at  $6^{\text{h}}7^{\text{m}}54^{\text{s}}.9$ ,  $-6^{\circ}21'57''$ , respectively, suggesting a jet axis at a position angle  $\approx 152^{\circ}$ . While there are a number of faint emission features to the north-east of the bipolar nebula, e.g., at  $6^{\text{h}}7^{\text{m}}48^{\text{s}}.8$ ,  $-6^{\circ}20'23''$ , no clear association of these features with the jet source can be established. We tentatively identify the bipolar nebula as the driving source of HOD07 12 based on its morphology. A much brighter star, also associated with extended emission at 2.12  $\mu\text{m}$  and in the Spitzer bands, and located at  $6^{\text{h}}7^{\text{m}}49^{\text{s}}.14$ ,  $-6^{\circ}20'33''$ ,



lies also on the jet axis and is surrounded by some  $2.12\ \mu\text{m}$  emission. It is the brightest source in the area on the Spitzer  $8.0\ \mu\text{m}$  image, indicating that it is a luminous, deeply embedded object.

### 3.4.13. HOD07 13

The nearly symmetric system of  $\text{H}_2$  shocks labeled HOD07 13 and located south of the Mon R2 cluster is the largest jet found in our survey. The center of the outflow HOD07 13 is clearly identifiable by an object on our S(1) image (Figs. 13 and 14) at position  $6^{\text{h}}7^{\text{m}}57^{\text{s}}.4$ ,  $-6^{\circ}31'6''$ . From this object, the northern jet extends along a position angle of  $\approx -13^{\circ}$ . Unfortunately, the available  $4.5\ \mu\text{m}$  and  $8.0\ \mu\text{m}$  Spitzer images do not extend sufficiently far south to include this object. However, all  $2.12\ \mu\text{m}$  features of this object are confirmed by the Spitzer  $3.6\ \mu\text{m}$  image (Fig. 13, right panel) that shows essentially the same outflow shock features.

A magnified view of the central region of this outflow is shown in Fig. 14. Immediately north of the central object, a faint string of emission knots is visible stretching about  $15''$  to the north. There is no counterpart to this knotty jet to the south of the central source, indicating the jet is inclined with its northern part towards the observer, and that the southern counterjet is obscured by molecular material surrounding the central source. However, the IRAC  $3.6\ \mu\text{m}$  image shows a faint outline of a paraboloid outflow cavity wall to the south.

More distant S(1) emission shock regions show a remarkable level of symmetry, since they are not affected by the obscuring material surrounding the central source. The first pair of emission regions are two complex regions, each showing two strands of emission knots, centered roughly at  $6^{\text{h}}7^{\text{m}}56^{\text{s}}.3$ ,  $-6^{\circ}29'39''$  (labeled 1N) and  $6^{\text{h}}7^{\text{m}}57^{\text{s}}.9$ ,  $-6^{\circ}32'23''$  (labeled 1S). Further out, we find a symmetric pair of fainter shock fronts at  $6^{\text{h}}7^{\text{m}}55^{\text{s}}.7$ ,  $-6^{\circ}29'4''$  (labeled 2N) and  $6^{\text{h}}7^{\text{m}}58^{\text{s}}.3$ ,  $-6^{\circ}32'56''$  (labeled 2S). The shock fronts farthest removed from the central source show substructure that is again similar in both the northern and southern jet: A symmetric pair of shock fronts at  $6^{\text{h}}7^{\text{m}}54^{\text{s}}.1$ ,  $-6^{\circ}27'33''$  (labeled 3N) and  $6^{\text{h}}8^{\text{m}}00^{\text{s}}.2$ ,  $-6^{\circ}34'30''$  (labeled 3S). Finally, the leading shock fronts are found at  $6^{\text{h}}7^{\text{m}}53^{\text{s}}.8$ ,  $-6^{\circ}27'19''$  (labeled 4N) and  $6^{\text{h}}8^{\text{m}}01^{\text{s}}.0$ ,  $-6^{\circ}34'43''$  (labeled 4S). The total projected length of this jet is  $\approx 7.5'$ , corresponding to  $1.8\ \text{pc}$ .

#### 3.4.14. *HOD07 14*

The compact, bipolar jet HOD07 14 (Fig. 15 and Fig. 16 top panel) is characterized by two bright shock fronts, at  $6^h7^m57^s.8$ ,  $-6^\circ25'26''$  and  $6^h8^m00^s.0$ ,  $-6^\circ25'40''$ , respectively, that define a jet axis at position angle  $\approx 114^\circ$ . The Spitzer  $4.5\ \mu\text{m}$  image (Fig. 16, top row, center) confirms the emission seen at  $2.12\ \mu\text{m}$ , but also shows additional emission, possibly indicative of a second jet parallel to HOD07 14, but more deeply embedded and therefore not visible in the near-infrared. The only indication of the position of the driving source of HOD07 14 is a flux minimum in the Spitzer  $8.0\ \mu\text{m}$  image, possibly a dense molecular clump seen in absorption against background emission. This argument would place the driving source at approximately  $6^h7^m58^s.9$ ,  $-6^\circ25'31''$ , the position listed in Table 1 and marked by a circle in Fig. 16.

#### 3.4.15. *HOD07 15*

The UKIRT S(1) image (Fig. 15) shows a nearly symmetric, bent system of shock fronts, with two bright shocks both to the north and south of the assumed position of the driving source. In addition, on each side, one fainter, extended shock is visible further away from the center of symmetry. The Spitzer  $4.5\ \mu\text{m}$  image (Fig. 16, bottom row, center) shows two additional emission knots in the jet, closer to the center, while the Spitzer  $8.0\ \mu\text{m}$  image shows a flux minimum in between those two strongly obscured  $4.5\ \mu\text{m}$  shocks. We identify this position, approximately  $6^h8^m10^s.0$ ,  $-6^\circ24'47''$ , as the position of the driving source of the jet HOD07 15 in Table 1 and Fig. 15.

### 3.5. Other Bipolar and Cometary Nebulae

The area near the Mon R2 cluster contains numerous small patches of nebulosity, often with bipolar or cometary morphology, that did not fit our criteria for identification as shocks or jets. We list those objects in Table 2 and indicate them by small square symbols in Figs. 1 and 2. The bipolar or cometary shape of many of these objects suggests that these are young, embedded stars still surrounded by disks and that they have just excavated an outflow cavity in the surrounding molecular material. These objects appear particularly numerous in the area about 2 to 3 arcminutes south of the main Mon R2 cluster, and just north of the cluster, as is demonstrated in Figs. 1 and 2. This finding is consistent with the result by Gutermuth (2005) that the Class I sources in Mon R2, identified by their J, H, and K, and Spitzer IRAC colors, are concentrated in a filamentary distribution to the south

of the cluster center, and to the north and north east of the cluster. While there is no strict relationship between reflection nebulae of bipolar or cometary morphology and SED Class I, the two criteria cover objects of similar evolutionary status at the trailing edge of their accretion phase. The main difference between the distribution of reflection nebulae and of the Class I sources identified by Gutermuth (2005) is that we find fewer individual reflection nebulae in the region dominated by the large, ring-like reflection nebula and the filamentary emission that dominates the center of the cluster. We attribute this difference largely to the difficulty of identifying small reflection nebulae around individual stars by morphological criteria in this crowded central region of the Mon R2 cluster.

By comparison, Gutermuth (2005) found that the older Class II sources, identified by J, H, and K-band colors, are more uniformly distributed around the Mon R2 cluster center, indicating a dynamically more relaxed population of more developed young stars.

## 4. OTHER INTERESTING OBJECTS IN THE FIELD

### 4.1. HH 866

The group of Herbig-Haro objects HH 866 found by Wang, Stecklum, & Henning (2005) in the L 1646 cloud was included in our field (Figs. 1 and 17). The HH objects are associated with the IRAS source 06046-0603. The region was identified by Carpenter (2000) as a region of enhanced star density in 2MASS data, and was identified as a potential CO outflow source by Xu et al. (2001). Our UKIRT/WFCAM  $2.12\ \mu\text{m}$  image shows a system of features that can be morphologically identified as likely  $\text{H}_2$  shocks.

The main system of emission knots in the center of Fig. 17 is extended roughly in north-south direction, and is probably physically associated with the bow shock at  $6^{\text{h}}7^{\text{m}}07^{\text{s}}.5$ ,  $-6^{\circ}04'36''$ . The position of the driving source of this jet cannot be determined with certainty. We tentatively list the center of symmetry of the brightest  $\text{H}_2$  emission knots at  $6^{\text{h}}7^{\text{m}}07^{\text{s}}.9$ ,  $-6^{\circ}03'42''$  as the position of the driving source, and name this jet HH 866 Jet W in Table 1. The central parts of this north-south jet are coinciding closely with knots A, B, and C in the  $\text{H}\alpha$  and  $[\text{SII}]$  images of Wang, Stecklum, & Henning (2005). To the east of this position is a large, rather poorly defined bow shock at  $6^{\text{h}}7^{\text{m}}08^{\text{s}}.1$ ,  $-6^{\circ}03'36''$  that appears to be associated with more shock emission knots further east of it. A plausible identification of the driving source is a star embedded in nebulosity at  $6^{\text{h}}7^{\text{m}}09^{\text{s}}.8$ ,  $-6^{\circ}03'44''$ . The nebulosity around this star was also noted by Wang, Stecklum, & Henning (2005) and the star is labeled "1" in their  $\text{H}\alpha$  image. Our image resolves this object into two stars, the eastern and fainter of which is associated with the nebulosity and is the likely outflow source. We list the position

of this star as HH 866 Jet E in Table 1.

#### 4.2. GGD 11

The bipolar reflection nebula GGD 11 (Gyulbudaghian, Glushkov, & Denisyuk 1978) was included in our UKIRT/WFCAM image and in Fig. 1. We show a more detailed view of this object in Fig. 18, because our image is, to our knowledge, the best available near-infrared image of GGD 11. This object has the typical morphology of a bipolar nebula, with the eastern lobe being far brighter than the western lobe, due to inclination of the object. The brightness distribution is fairly smooth, in contrast to the knotty and filamentary appearance of typical H<sub>2</sub> jets.

#### 4.3. NGC 2182

The NGC 2182 reflection nebula was included in our UKIRT/WFCAM image even though it is not included the image section shown in Fig. 1. It is shown in detail in Fig. 19. Different from the smooth appearance of this object on optical photographs, e. g. on the red plate of the DSS2, and on the K-band 2MASS image, the UKIRT 2.12  $\mu\text{m}$  S(1) image shows two filamentary regions of enhanced S(1) line emission to the west of the illuminating star. We cannot determine the excitation mechanism of these two filaments just from one image and both fluorescent excitation and shock excitation are possible.

### 5. COMPARISON WITH OTHER STAR FORMING REGIONS

In our 2.12  $\mu\text{m}$  imaging survey of the Mon R2 molecular cloud for H<sub>2</sub> jets associated with forming stars, we have found a total of 15 new H<sub>2</sub> jets in Mon R2 and two additional H<sub>2</sub> jets in the L 1646 (HH 866) region. Together with the two outflows detected in CO by Tafalla et al. (1997) and the IRS 3 microjet found by Preibisch et al. (2002) this gives a minimum of 20 active jets and outflows in the larger area of Mon R2 (including the L 1646 region), in addition to the huge, but probably inactive, CO outflow found by Loren (1981). The spatial distribution of the H<sub>2</sub> jets in Mon R2 along the projected edge of the large CO outflow, in particular the cluster of H<sub>2</sub> jets 12' north of the Mon R2 main cluster, suggests that this star-formation activity was triggered by the huge fossil CO outflow in Mon R2, one of the largest outflows known.

By comparison, in a similar survey of Orion A, Stanke, McCaughrean, & Zinnecker

(2002) found 44 jets with a high degree of certainty, and 29 less certain cases. Considering that their survey area was larger than ours, and the Orion A cloud is more massive than the Mon R2 cloud, this comparison implies a similar specific star formation rate in both clouds. The level of outflow activity in Mon R2 is also similar to that found in the two massive star-forming regions DR21 and W75, where Davis et al. (2007) found a combined number of approximately 50  $\text{H}_2$  jet sources based on a similar UKIRT WFCAM.

NGC 1333 is one of the most active star-forming regions in the solar vicinity and Bally, Devine, & Reipurth (1996) list 15 optical Herbig-Haro objects,  $\text{H}_2$  jets, and CO outflows in this region. This region is closer to the Sun than the other regions discussed before, and the discovery of jets is therefore easier. In the Perseus molecular cloud as a whole, of which NGC 1333 is a part, Walawender et al. (2005) counted a total of 141 optically ( $\text{H}\alpha$  and [SII]) detectable Herbig-Haro objects that, at the minimum, belong to 30 individual outflows. The smaller Barnard 1 cloud ( $\approx 1200 \text{ M}_\odot$ ) was found by Walawender et al. (2005b) to have 8 protostars driving outflows. Also, Bally et al. (2006) found a total of at least 20 outflows in the Chamaeleon I molecular cloud, mostly by an optical search supported by Spitzer data. Chamaeleon I is a nearby (165 pc), relatively low-mass ( $1000 \text{ M}_\odot$ ) cloud. In light of the different techniques used to search for collimated jets from young stars in these different regions, we conclude that the number of such jets discovered in Mon R2 is similar to that found in the other massive star forming regions.

While it may be argued that the presence of reflection nebulosity, fluorescently excited  $\text{H}_2$  emission and PAH emission makes the discovery of shock-excited  $\text{H}_2$  emission near the central cluster of Mon R2 difficult, this is also the region most intensely studied in the past, and only the IRS 3 microjet was found there. By contrast, most of our newly discovered jets are located in the periphery of the central cluster, and the longest collimated jets were found farthest away from the central cluster. The complete absence of large  $\text{H}_2$  jets near the center of the Mon R2 cluster cannot be explained by observational selection effects alone and suggests that  $\text{H}_2$  jets do not form in this environment.

This is in agreement with the finding by Davis et al. (2007) in DR21/W75 who conclude that the  $\text{H}_2$  jets in their sample are usually not associated with young molecular cores detectable at sub-mm wavelengths or with compact infrared clusters. They further conclude that clustering may inhibit disc accretion and the production of extensive flows. A similar conclusion can also be drawn from the extensive survey of the Orion A cloud for  $\text{H}_2$  jets by Stanke, McCaughrean, & Zinnecker (2002). In Orion A,  $\text{H}_2$  jets are predominantly found outside the area of the Trapezium cluster and the Orion nebula. Also, Hodapp (1994) noted in their K' imaging survey of CO outflow sources that member objects of large young clusters are less likely to show jets, or localized reflection nebulosity than young objects in smaller

groupings.

## 6. Conclusions

Our UKIRT WFCAM imaging survey of the Mon R2 molecular cloud for  $\text{H}_2$  jets associated with forming stars was based on a  $2.12\ \mu\text{m}$   $\text{H}_2$  1–0 S(1) plus continuum image. Object identification was based on morphology and confirmation by archival Spitzer images. We have found a total of 17 new  $\text{H}_2$  jets, including the two in L 1646, as well as 27 small reflection nebulae.

We conclude that the number of  $\text{H}_2$  jet sources in Mon R2 is similar to that found in other star forming regions of comparable size. We note that the  $\text{H}_2$  jets appear to be concentrated in projection against the walls of the outflow cavity created by the large Mon R2 CO outflow. This is indicative of a scenario of sequential star formation in Mon R2 triggered by the large outflow.

We confirm the finding in other high-mass star forming regions that  $\text{H}_2$  jets tend to be found outside of the dense central cluster in such regions. It appears that the environment of a dense cluster containing some massive stars prevents the formation of large  $\text{H}_2$  jets.

The United Kingdom Infrared Telescope is operated by the Joint Astronomy Centre on behalf of the U.K. Particle Physics and Astronomy Research Council.

This work is based in part on observations made with the Spitzer Space Telescope, which is operated by the Jet Propulsion Laboratory, California Institute of Technology under a contract with NASA.

This publication makes use of data products from the Two Micron All Sky Survey, which is a joint project of the University of Massachusetts and the Infrared Processing and Analysis Center / California Institute of Technology, funded by the National Aeronautics and Space Administration and the National Science Foundation.

## REFERENCES

- Andersen, M., Meyer, M. R., Oppenheimer, B., Dougados, C. & Carpenter, J. 2006, AJ, 132, 2296
- André, P., Ward-Thompson, D., & Barsony, M. 1993, ApJ, 406, 122
- Bally, J., Devine, D., & Reipurth, B. 1996, ApJ, 473, L49
- Bally, J., Walawender, J., Luhman, K. L., & Fazio, G. 2006, AJ, 132, 1923
- Bate, M. R., Bonnell, I. A., Clarke, C. J., Lubow, S. H., Ogilvie, G. I., Pringle, J. E., & Tout, C. A. 2000, MNRAS, 317, 773
- Beckwith, S., Evans, N. J., Becklin, E. e., & Neugebauer, G. 1976, ApJ, 208, 390
- Black, J. H. & Dalgarno, A. 1976, ApJ, 203, 132
- Carpenter, J. M. 2000, AJ, 120, 3139
- Carpenter, John M., Meyer, Michael R., Dougados, Catherine, Strom, Stephen E., Hillenbrand, Lynne A. 1997, AJ114, 198
- Casali, M., Adamson, A., Alves de Oliveira, C., Almaini, O., Burch, K., Chuter, T., Elliot, J., Folger, M., Foucaud, S., Hambly, N., Hastie, M., Henry, D., Hirst, P., Irwin, M., Ives, D., Lawrence, A., Laidlaw, K., Lee, D., Lewis, J., Lunney, D., Mclay, S., Montgomery, D., Pickup, A., Read, M., Rees, N., Robson, I., Sekiguchi, K., Vick, A., Warren, S., & Woodward, B. 2007, A&A, 777
- Cohen, J. G. & Frogel, J. A. 1977, ApJ, 211, 178
- Choi, M., Evans, Neal J. II, Tafalla, M., & Bachiller, R. 2000, ApJ, 538, 738
- Davis, C. J., Kumar, M. S. N., Sandell, G., Froebrich, D., Smith, M. D., & Currie, M. J. 2007, MNRAS, 374, 29
- Dye, S. et al. 2006, MNRAS, 372, 1227
- Fazio, G. G. et al. 2004, ApJS, 154, 10
- Giannakopoulou, J., Mitchell, G. F., Hasegawa, T. I., Matthews, H. E., & Maillard, J.-P. 1997, ApJ, 487, 346
- Gyulbudaghian, A. L., Glushkov, Y. L., & Denisjuk, E. K. 1978, ApJ, L137

- Gutermuth, R. A. 2005, Ph.D. Thesis, University of Rochester
- Herbst, W. & Racine, R. 1976, *AJ*, 81, 840
- Hodapp, K.-W. 1987, *A&A*, 172, 304
- Hodapp, K.-W. 1994, *ApJS*, 94, 615
- Hodapp, K.-W. & Ladd, E. F. 1995, *ApJ*, 453, 715
- Hodapp, K. W. & Davis, C. J. 2002, *ApJ*, 575, 291
- Hodapp, K. W., Bally, J., Eisloffel, J., & Davis, C. J. 2005, *AJ*, 129, 1580
- Jarrett, T. H., Novak, G., Xie, T., & Goldsmith, P. F. 1994, *ApJ*, 430, 743
- Kumar, M. S. N., Davis, C. J., Grave, J. M. C., Ferreira, B., & Froebrich, D. 2007, *MNRAS*, 373, 54
- Loren, R. B. 1981, *ApJ*, 249, 550
- Maddalena, R. J., Morris, M., Moscowitz, J., & Thaddeus, P. 1986, *ApJ*, 303, 375
- Meyers-Rice, B. A. & Lada, C. J. 1991, *ApJ*, 368, 445
- Preibisch, T., Balega, Y. Y., Schertl, D., & Weigelt, G. 2002, *A&A*, 392, 945
- Ridge, N. A., Wilson, T. L., Megeath, S. T., Allen, L. E. & Myers, P. C. 2003, *AJ*, 126, 286
- Skrutskie, M. F., Cutri, R. M., Stiening, R., Weinberg, M. D., Schneider, S., Carpenter, J. M., Beichman, C., Capps, R., Chester, T., Elias, J., Huchra, J., Liebert, J., Lonsdale, C., Monet, D. G., Price, S., Seitzer, P., Jarrett, T., Kirkpatrick, J. D., Gizis, J., Howard, E., Evans, T., Fowler, J., Fullmer, L., Hurt, R., Light, R., Kopan, E. L., Marsh, K. A., McCallon, H. L., Tam, R., Van Dyk, S., & Wheelock, S. 2006, *AJ*, 131, 1163
- Shull, J. M. & Hollenback, D. J. 1978, *ApJ*, 220, 525
- Smith, M. D. & Rosen, A. 2005, *MNRAS*, 357, 1370
- Smith, H. A., Hora, J. L., Marengo, M., & Pipher, J. L. 2006, *ApJ*, 645, 1264
- Stanke, T., McCaughrean, M. J., & Zinnecker, H. 2002, *A&A*, 392, 239
- Tafalla, M., Bachiller, R., Wright, M. C. H., & Welch, W. J. 1997, *ApJ*, 474, 329



- Terquem, C., Eislöffel, J., Papaloizou, J. C. B., & Nelson, R. P. 1999, *ApJ*, 512, L131
- van den Bergh, S. 1966, *AJ*, 71, 990
- Walawender, J., Bally, J., & Reipurth, B. 2005, *AJ*, 129, 2308
- Walawender, J., Bally, J., Kirk, H., & Johnstone, D. 2005, *AJ*, 130, 1795
- Wang, H., Stecklum, B., & Henning, Th. 2005, *A&A*, 437, 169
- Wolf, G. A., Lada, C. J., & Bally, J. 1990, *AJ*, 100, 1892
- Xu, Y., Jiang, D.-R., Yu, Z.-Y. et al. 2001, *ChJAA*, 1, 60

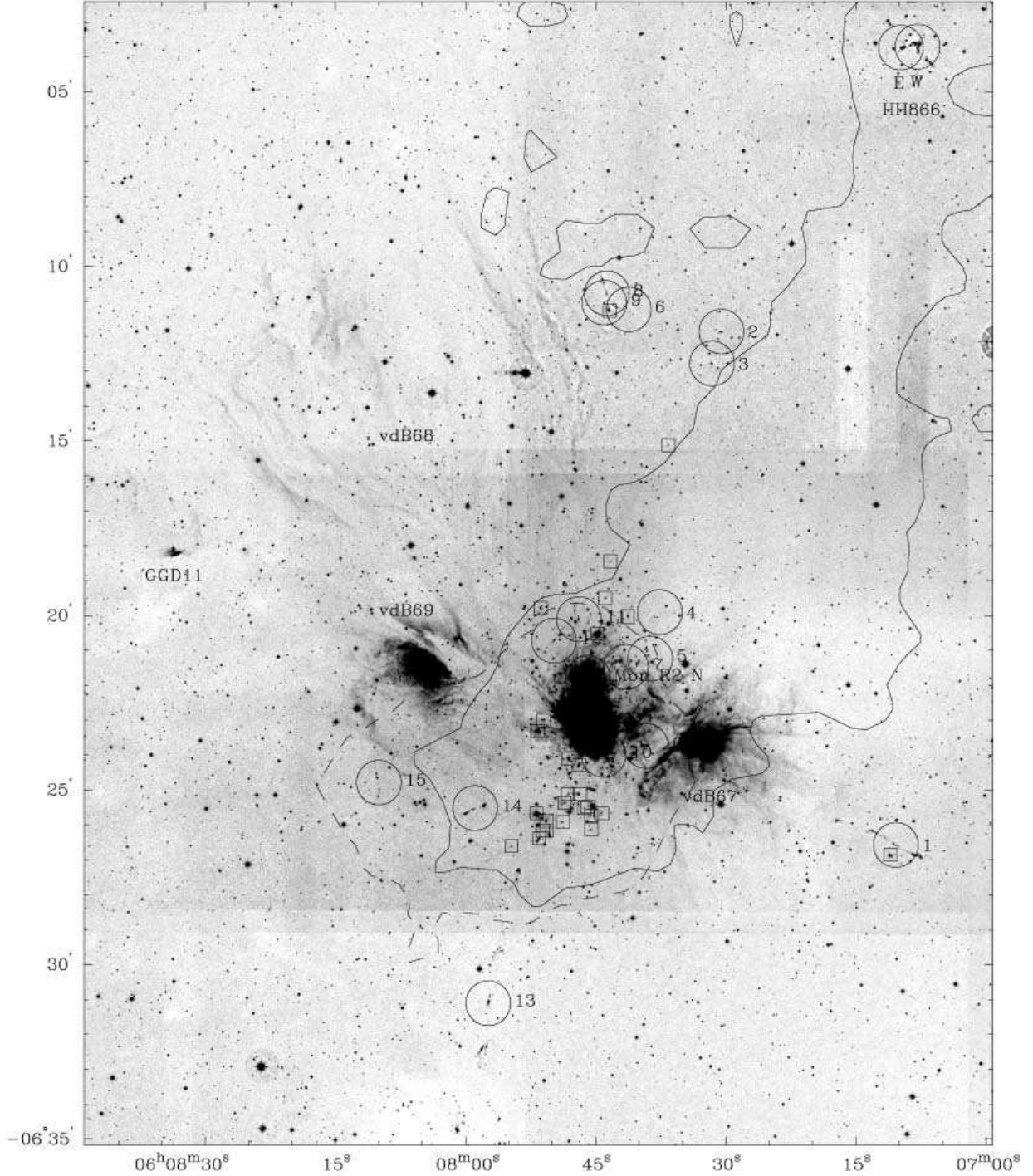


Fig. 1.— Image of the Mon R2 star forming region in the 1–0 S(1) emission line of  $\text{H}_2$  at  $2.12 \mu\text{m}$ , obtained with the WFCAM at UKIRT. The circles indicate the positions of the newly found  $\text{H}_2$  jets. The Herbig-Haro object HH 866 is visible in the north-west corner of the image. The small reflection nebula near the eastern edge of the image is GGD 11 (Gyulbudaghian, Glushkov, & Denisyuk 1978). Newly found small reflection nebulae are indicated by squares. Superposed on this image are lowest contours of the blueshifted ( $-2$  to  $6 \text{ km s}^{-1}$ , solid line) and redshifted ( $14$  to  $22 \text{ km s}^{-1}$ , dashed line) CO emission from the map by Wolf et al. (1990).

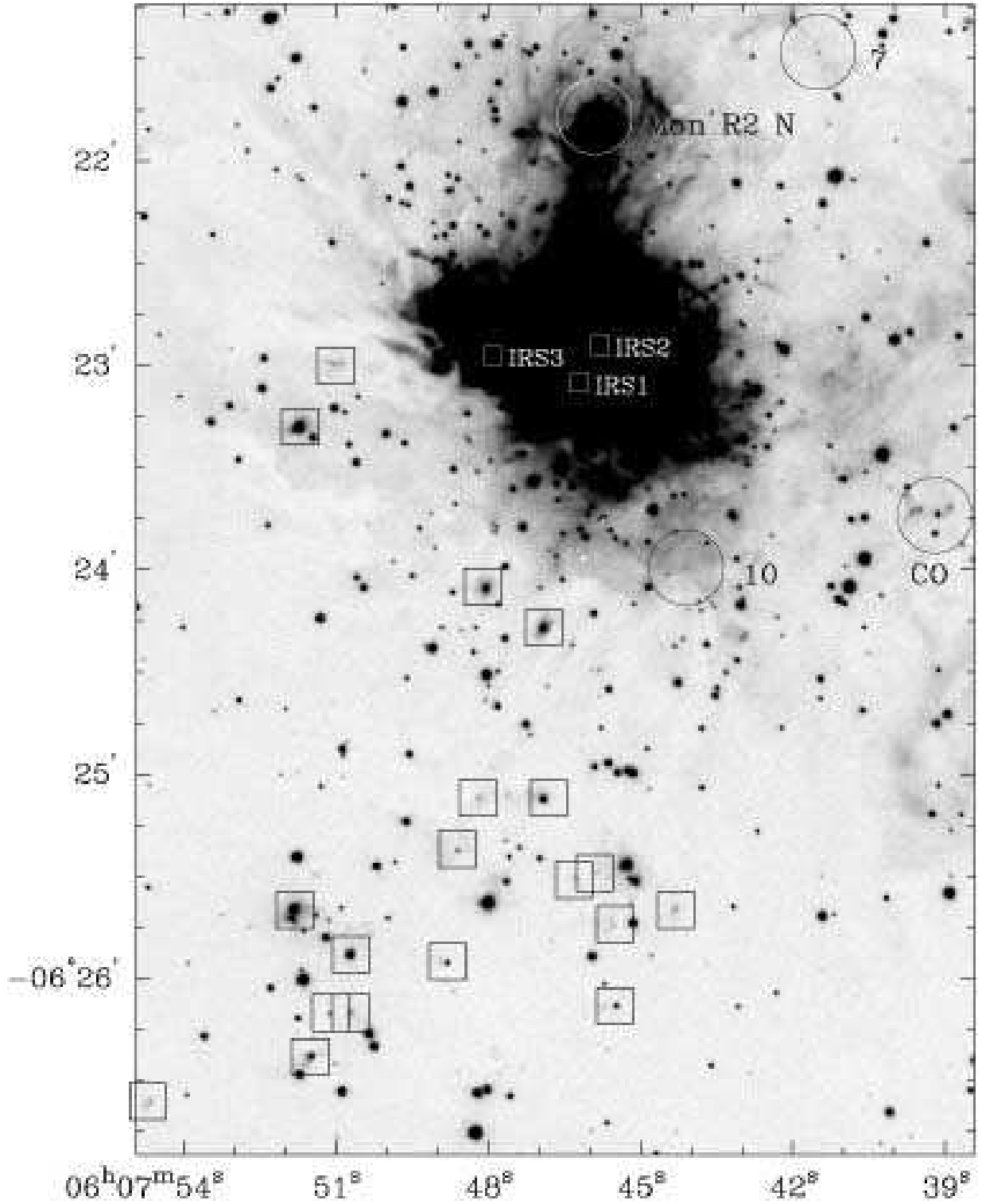


Fig. 2.— A detailed view of the Mon R2 center region, based on the same UKIRT/WFCAM 2.12  $\mu\text{m}$  S(1) line + continuum image as Fig. 1. The two CO outflows identified by Tafalla et al. (1997), Mon R2 N and CO 100,-40, are indicated, as well as the newly found outflows HOD07 7 and 10. The positions of the three dominant infrared sources, IRS 1 - 3 (Beckwith et al. 1976), are indicated in the overexposed central region of the Mon R2 cluster. The positions of many of the small reflection nebulae from Table 2 are indicated by squares.

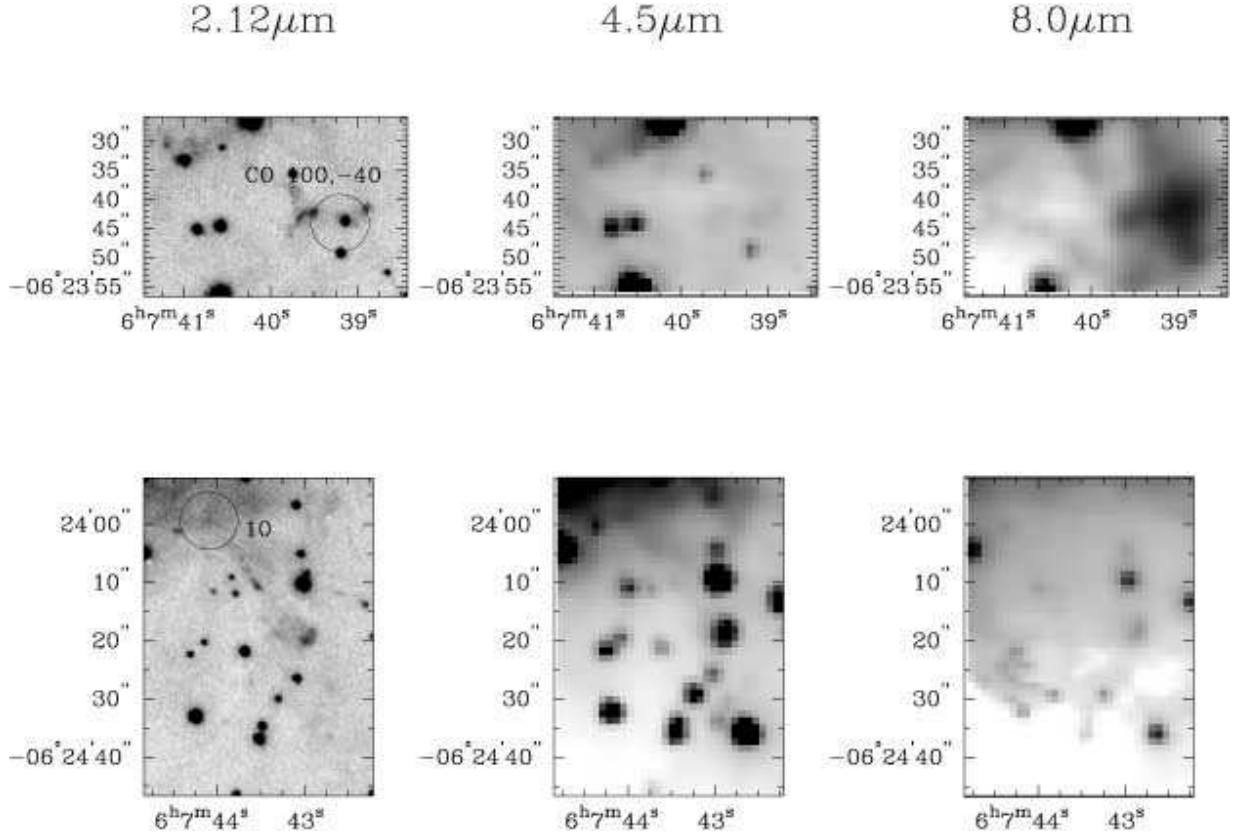


Fig. 3.— This figure shows detailed views of the two outflows in the Mon R2 center region in the 2.12  $\mu\text{m}$  S(1) line + continuum, Spitzer IRAC 4.5  $\mu\text{m}$ , and Spitzer IRAC 8.0  $\mu\text{m}$  bands. The top panels show the outflow CO 100,-40 (Tafalla et al. 1997), the bottom panels the outflow HOD07 10.

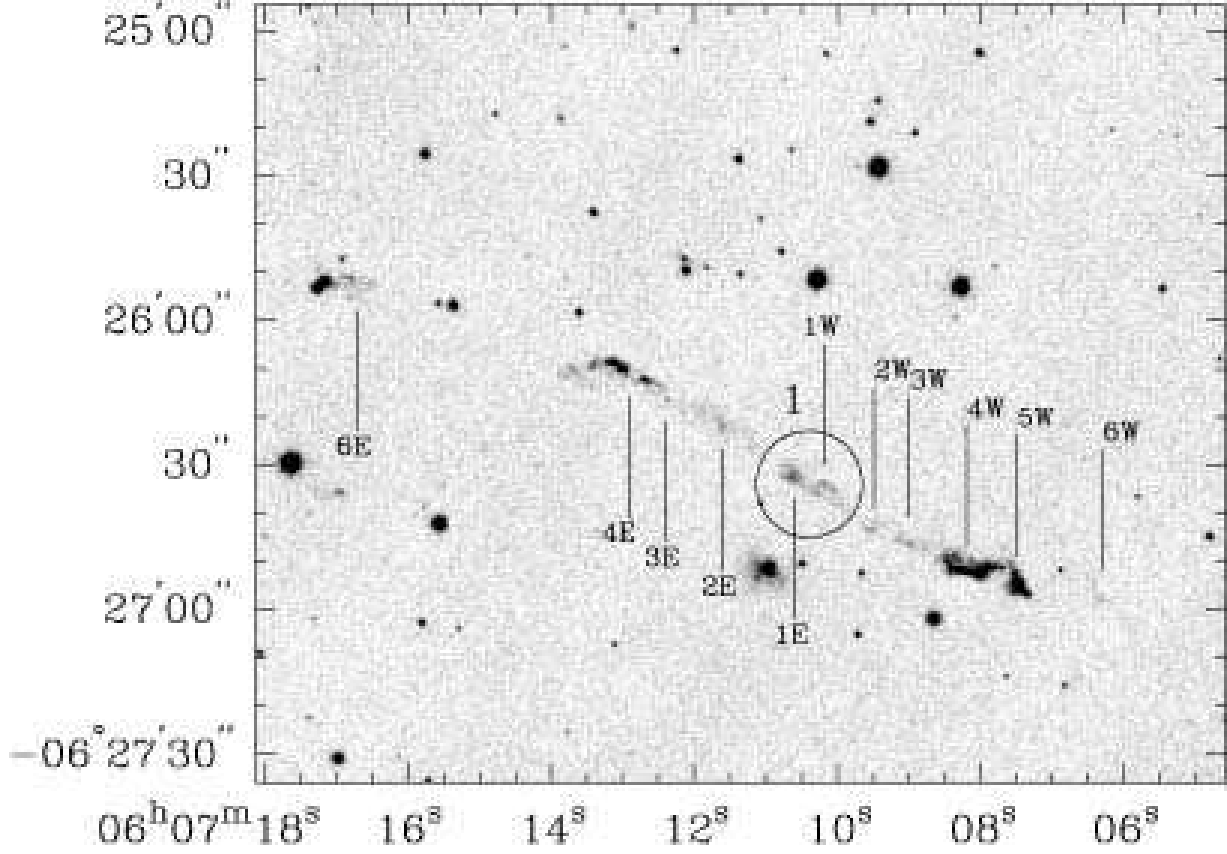


Fig. 4.— This 2.12  $\mu\text{m}$  S(1) line + continuum image shows outflow HOD07 1. The tentative outflow center (marked by a circle) is located at  $6^{\text{h}}7^{\text{m}}10^{\text{s}}.4$ ,  $-6^{\circ}26'34''$  in the flux minimum between the two patches of nebulosity that define the center of symmetry. The symmetric sets of shocks in the western and eastern jet are labeled.

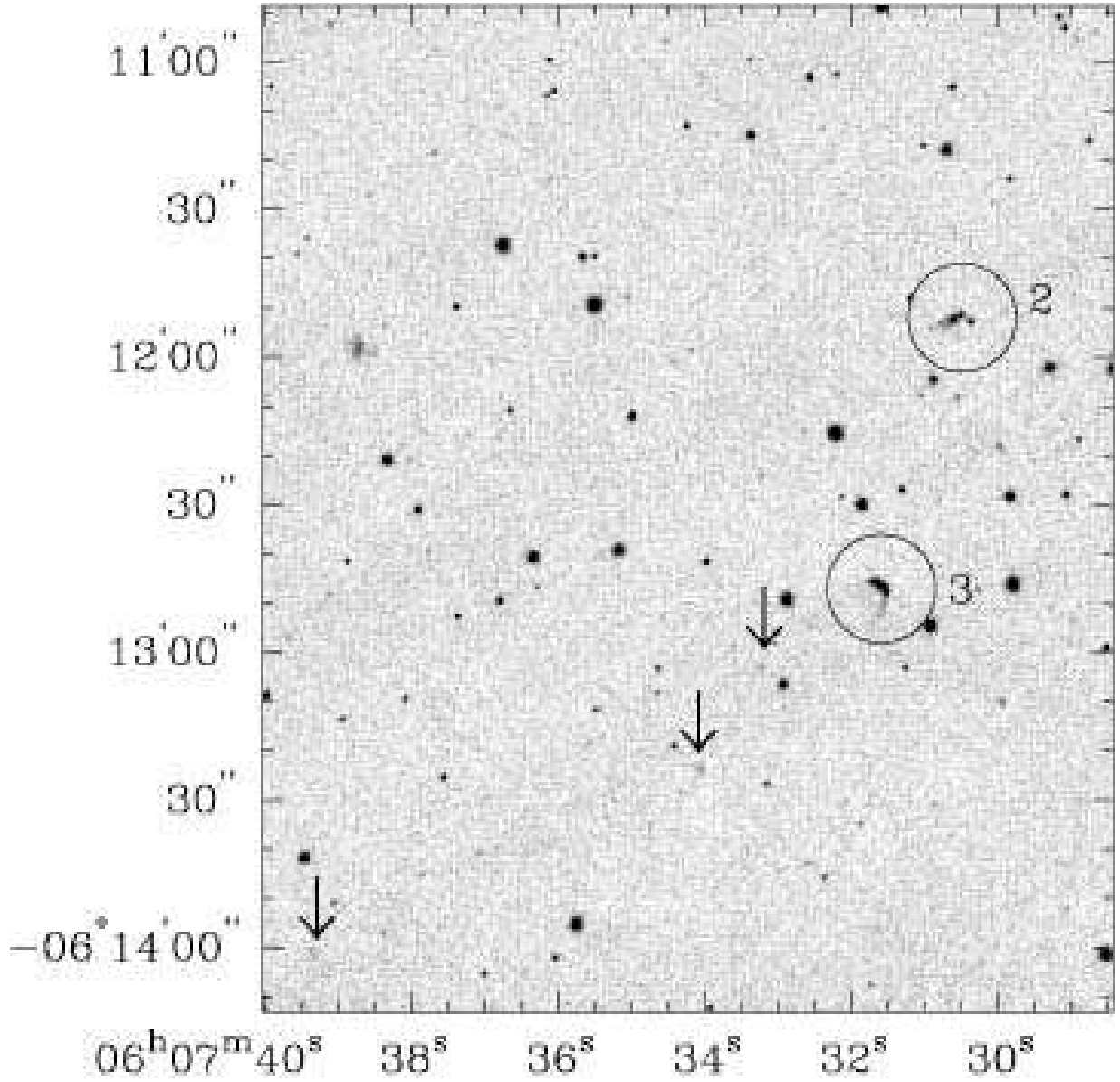


Fig. 5.— This figure shows the  $2.12\ \mu\text{m}$  image of two separate systems of  $\text{H}_2$  knots: HOD07 2 at  $6^{\text{h}}7^{\text{m}}30^{\text{s}}.5$ ,  $-6^\circ11'51''$  is likely a small jet with several internal shocks. The bow shock HOD07 3 is located at  $6^{\text{h}}7^{\text{m}}31^{\text{s}}.6$ ,  $-6^\circ12'46''$ . Projecting back from the bow shock along its plausible jet axis, we find a string of faint, slightly extended knots of emission that are also visible on the Spitzer  $4.5\ \mu\text{m}$  image. These faint emission features, indicated by arrows in Fig. 5, are located at  $6^{\text{h}}7^{\text{m}}33^{\text{s}}.2$ ,  $-6^\circ13'03''$ , at  $6^{\text{h}}7^{\text{m}}34^{\text{s}}.1$ ,  $-6^\circ13'24''$ , and at  $6^{\text{h}}7^{\text{m}}39^{\text{s}}.3$ ,  $-6^\circ14'01''$ . Overall, they appear to form a jet with multiple, faint internal shocks, ending in the bright bow shock.

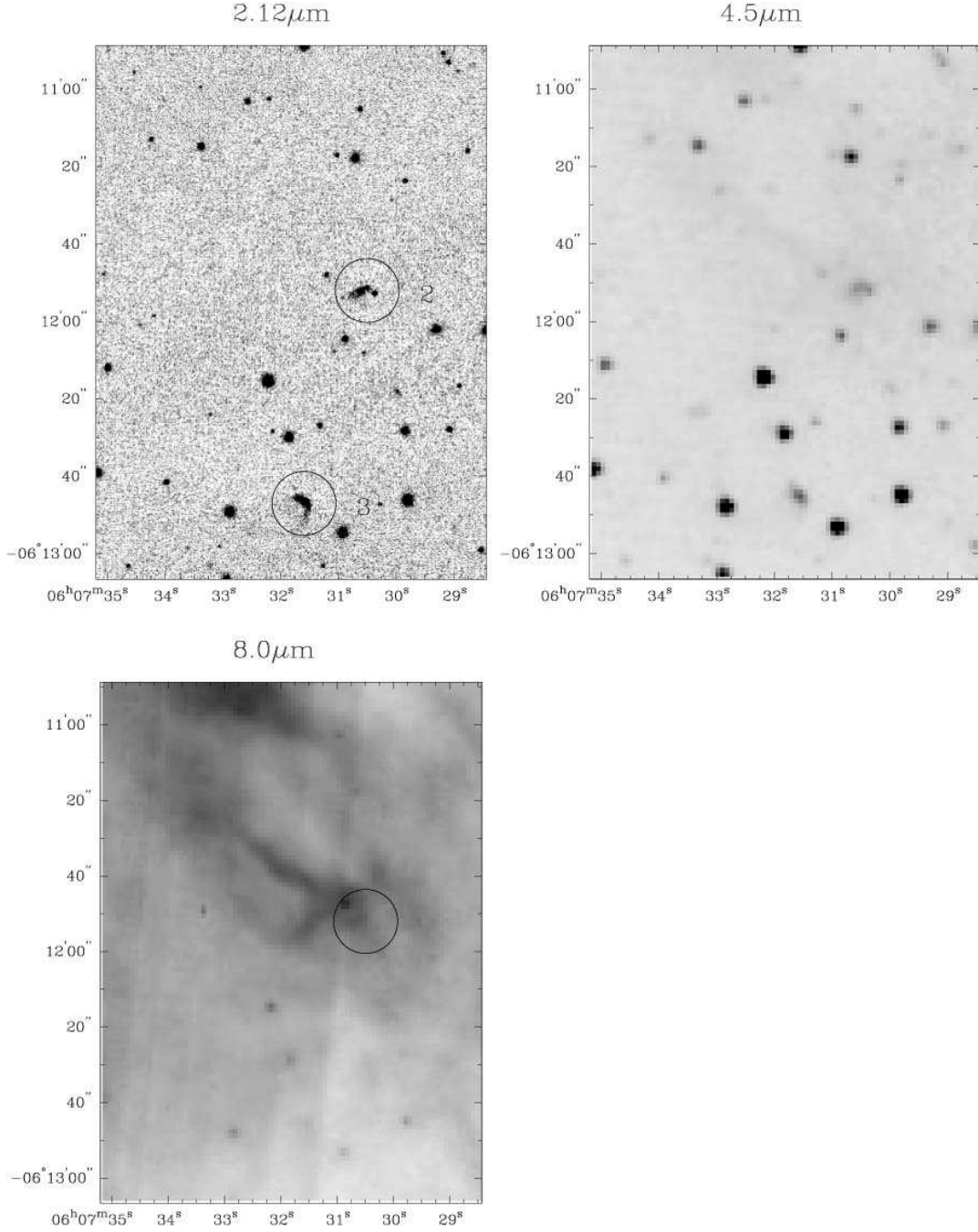


Fig. 6.— This figure compares the  $2.12\mu\text{m}$ , IRAC  $4.5\mu\text{m}$  and  $8.0\mu\text{m}$  images of two separate systems of  $\text{H}_2$  knots: HOD07 2 at  $6^{\text{h}}7^{\text{m}}30^{\text{s}}.5$ ,  $-6^{\circ}11'51''$  is a small jet with several internal shocks and the position given is that of the most compact knot. The  $8.0\mu\text{m}$  Spitzer image shows extended nebulosity and a point source that, however, cannot be identified as the central source of the jet. The bow shock HOD07 3 is located at  $6^{\text{h}}7^{\text{m}}31^{\text{s}}.6$ ,  $-6^{\circ}12'46''$ . The driving source of this bow shock could not be identified.

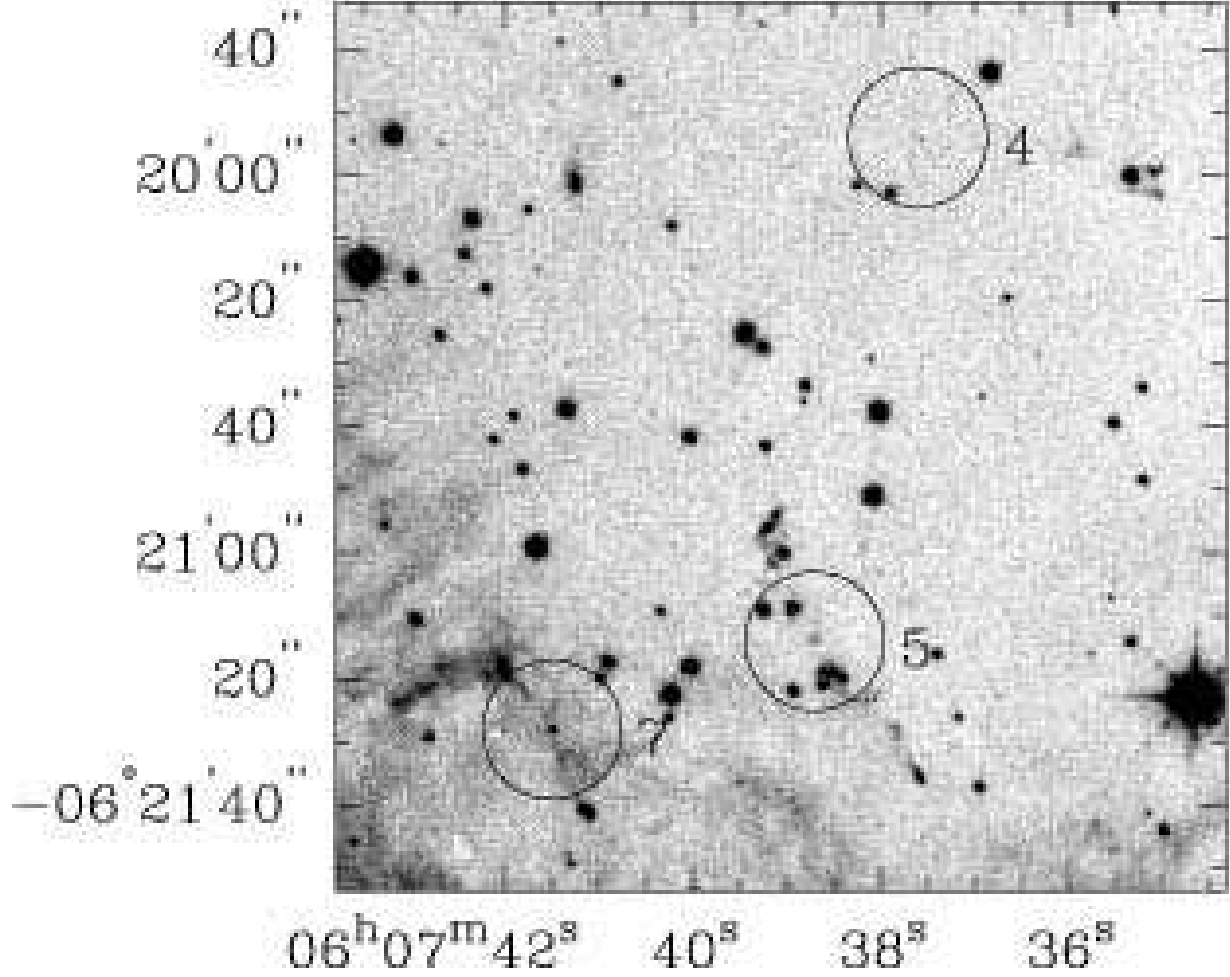


Fig. 7.— This  $2.12\ \mu\text{m}$  S(1) line + continuum image contains 3 separate systems of  $\text{H}_2$  knots: HOD07 4 at  $6^{\text{h}}7^{\text{m}}35^{\text{s}}3$ ,  $-6^\circ20'0''$ , appears as a star with nebulous knots. As shown in Fig. 8, this position is most likely not the central source of this outflow. HOD07 5 at  $6^{\text{h}}7^{\text{m}}38^{\text{s}}7$ ,  $-6^\circ21'14''$ , is the likely central star of this bipolar jet. HOD07 7 at  $6^{\text{h}}7^{\text{m}}41^{\text{s}}5$ ,  $-6^\circ21'28''$ , is the likely position of the outflow center of that jet.



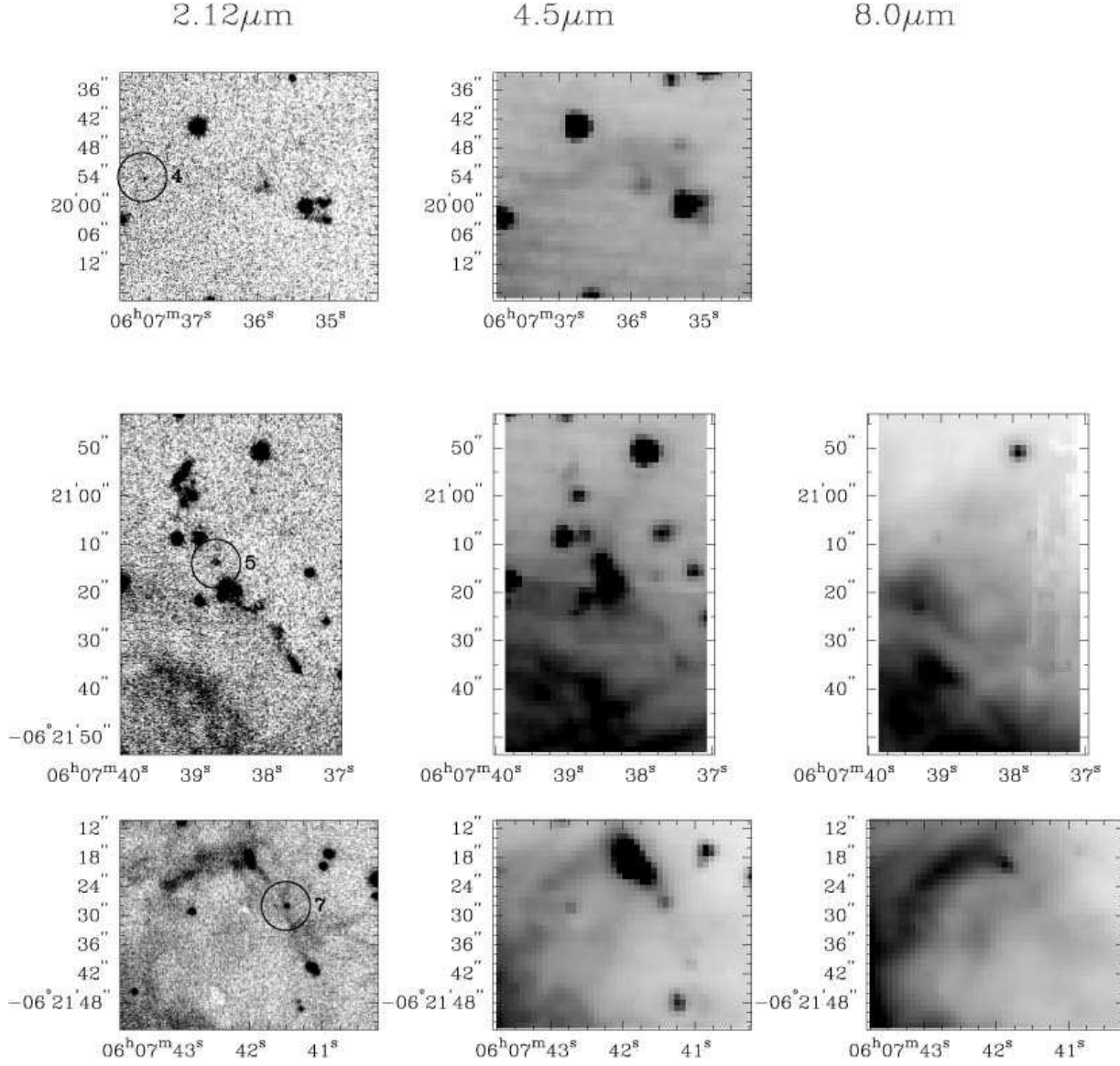


Fig. 8.— This figure contains the  $2.12\mu\text{m}$  S(1),  $4.5\mu\text{m}$  and  $8.0\mu\text{m}$  images of the three systems of H<sub>2</sub> knots found in the area of Fig. 7: The driving source of HOD07 4 is probably located at  $6^{\text{h}}7^{\text{m}}37^{\text{s}}6$ ,  $-6^{\circ}19'54''$ , marked by a very faint star and the apex of the jet-like nebulosity of the Spitzer  $4.5\mu\text{m}$  image. HOD07 5 lies at  $6^{\text{h}}7^{\text{m}}38^{\text{s}}7$ ,  $-6^{\circ}21'14''$ , identified by a faint source at the approximate center of symmetry of the bipolar jet. HOD07 7 at  $6^{\text{h}}7^{\text{m}}41^{\text{s}}5$ ,  $-6^{\circ}21'28''$ , is the likely position of the driving source of a bipolar jet.

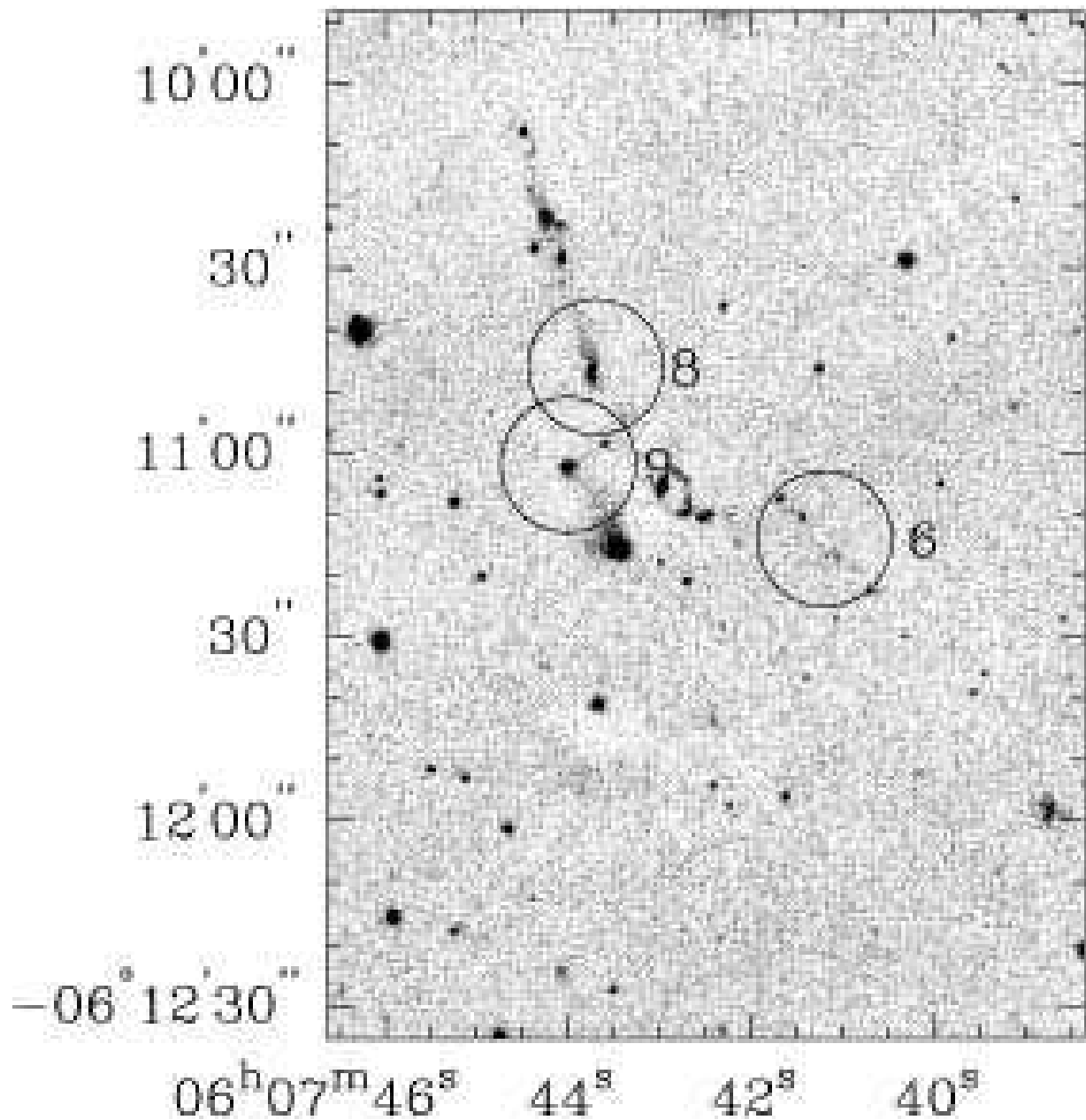


Fig. 9.— This  $2.12\ \mu\text{m}$  S(1) line + continuum image contains 3 separate systems of  $\text{H}_2$  knots: HOD07 6 at  $6^{\text{h}}07^{\text{m}}41^{\text{s}}.2$ ,  $-6^\circ11'14''$  is the center of symmetry of a string of emission knots. HOD07 8 at  $6^{\text{h}}07^{\text{m}}43^{\text{s}}.7$ ,  $-6^\circ10'46''$  is the likely center of a single-sided jet. HOD07 9 at  $6^{\text{h}}07^{\text{m}}44^{\text{s}}.0$ ,  $-6^\circ11'2''$  is a star associated with  $\text{H}_2$  emission and the likely source of a bow shock.

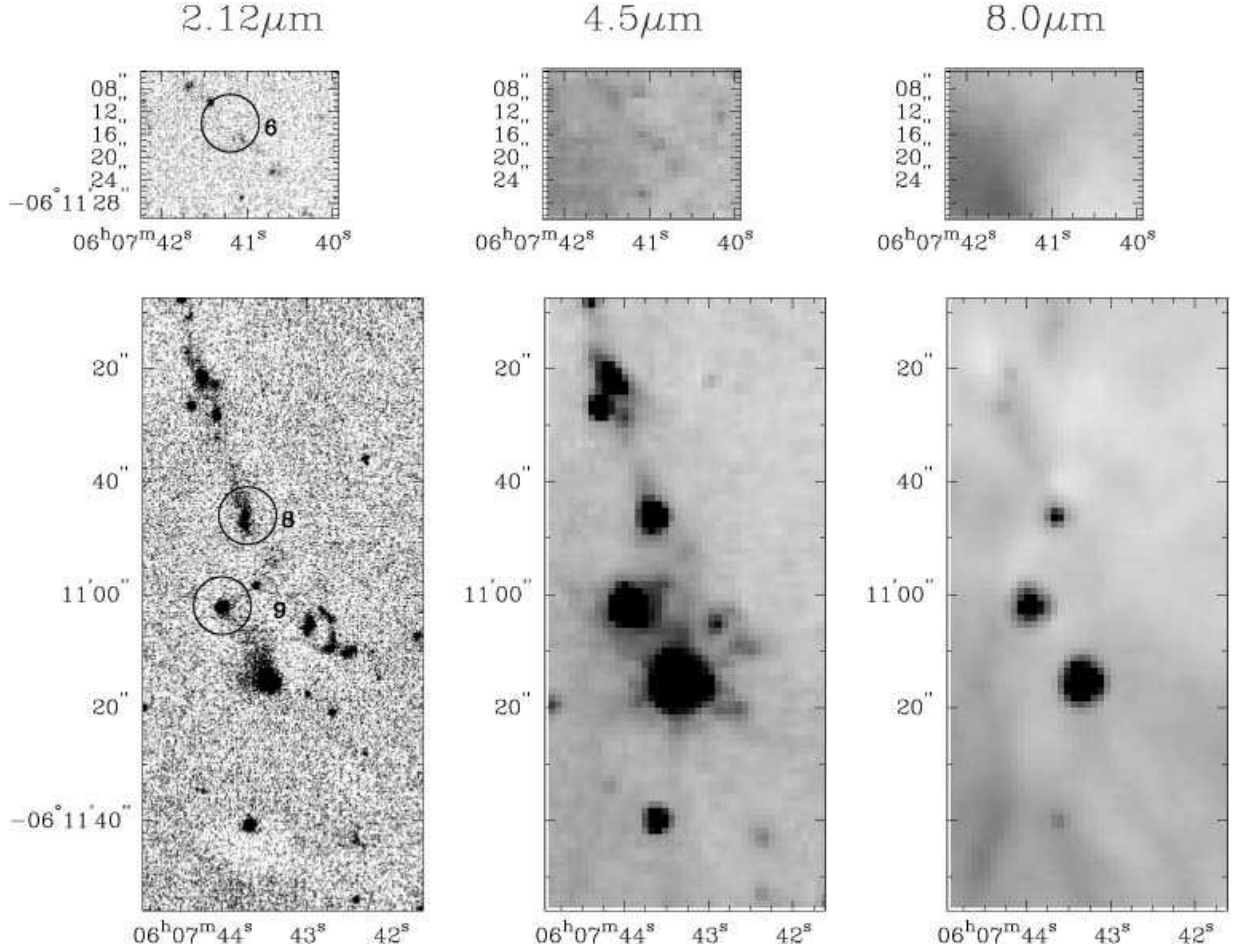


Fig. 10.— This figure shows the S(1), 4.5  $\mu\text{m}$ , and 8.0  $\mu\text{m}$  images of three systems of  $\text{H}_2$  knots: In the top row, HOD07 6 at  $6^{\text{h}}7^{\text{m}}41^{\text{s}}.2$ ,  $-6^{\circ}11'14''$  is the center of symmetry of a string of emission knots. In the bottom row, HOD07 8 at  $6^{\text{h}}7^{\text{m}}43^{\text{s}}.7$ ,  $-6^{\circ}10'46''$  is the likely center of a single-sided jet. HOD07 9 at  $6^{\text{h}}7^{\text{m}}44^{\text{s}}.0$ ,  $-6^{\circ}11'2''$  is a star associated with  $\text{H}_2$  emission and the likely source of a bow shock.

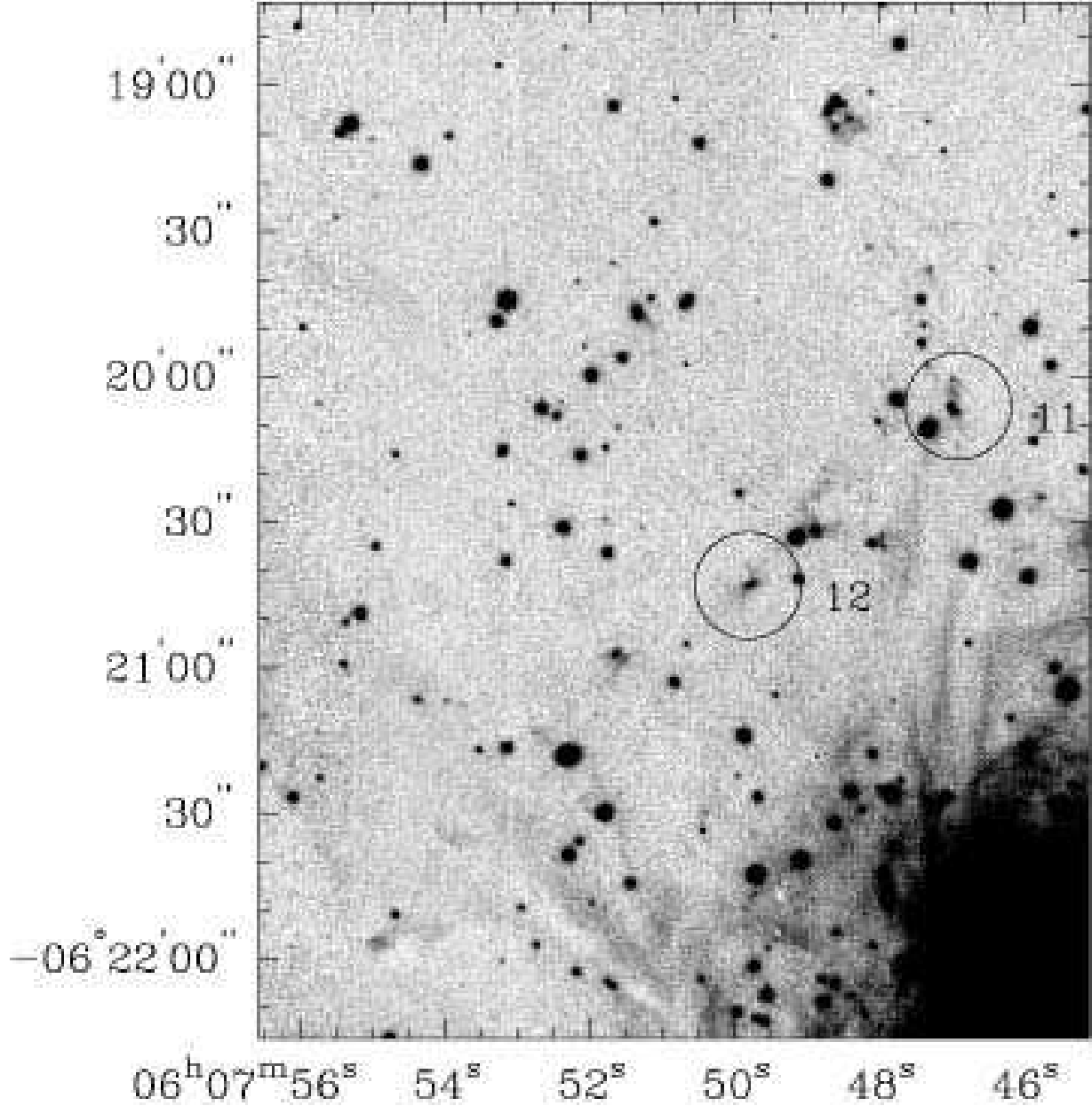


Fig. 11.— This figure is a  $2.12\ \mu\text{m}$  S(1) line + continuum image and contains two separate systems of  $\text{H}_2$  knots: The circle identifying HOD07 11 at  $6^{\text{h}}7^{\text{m}}46^{\text{s}}9$ ,  $-6^\circ20'6''$  marks the putative position of the central source of a jet extending to the north-north-east (P.A.  $\approx 23^\circ$ ) and ending in a well-defined bow shock located at  $6^{\text{h}}7^{\text{m}}48^{\text{s}}6$ ,  $-6^\circ19'3''$ . Several fainter knots of S(1) emission lie between the center and the bow shock, completing the morphology of a typical jet. The object HOD07 12 at  $6^{\text{h}}7^{\text{m}}49^{\text{s}}8$ ,  $-6^\circ20'43''$  has the morphology of a faint bipolar nebula. Two other knots of S(1) emission lie to the south-east at  $6^{\text{h}}7^{\text{m}}51^{\text{s}}6$ ,  $-6^\circ20'58''$  and at  $6^{\text{h}}7^{\text{m}}54^{\text{s}}9$ ,  $-6^\circ21'57''$ , respectively. While there are a number of faint features to the north-east of the bipolar nebula, no clear association with this jet source can be established.

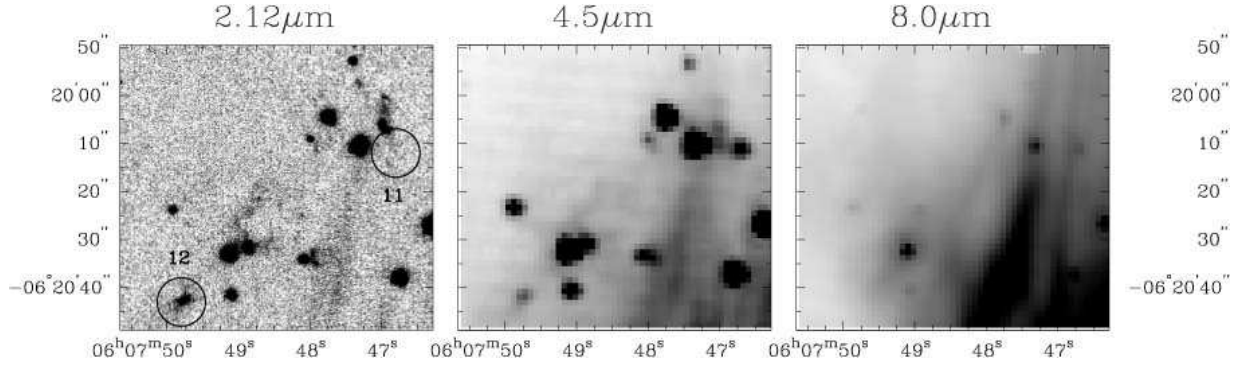


Fig. 12.— This figure shows images in 2.12  $\mu\text{m}$  S(1), 4.5  $\mu\text{m}$ , and 8.0  $\mu\text{m}$  of the central region of the two outflow sources shown in Fig. 11: HOD07 11 at  $6^{\text{h}}07^{\text{m}}46^{\text{s}}8$ ,  $-6^{\circ}20'12''$  and HOD07 12 at  $6^{\text{h}}07^{\text{m}}49^{\text{s}}8$ ,  $-6^{\circ}20'43''$ .

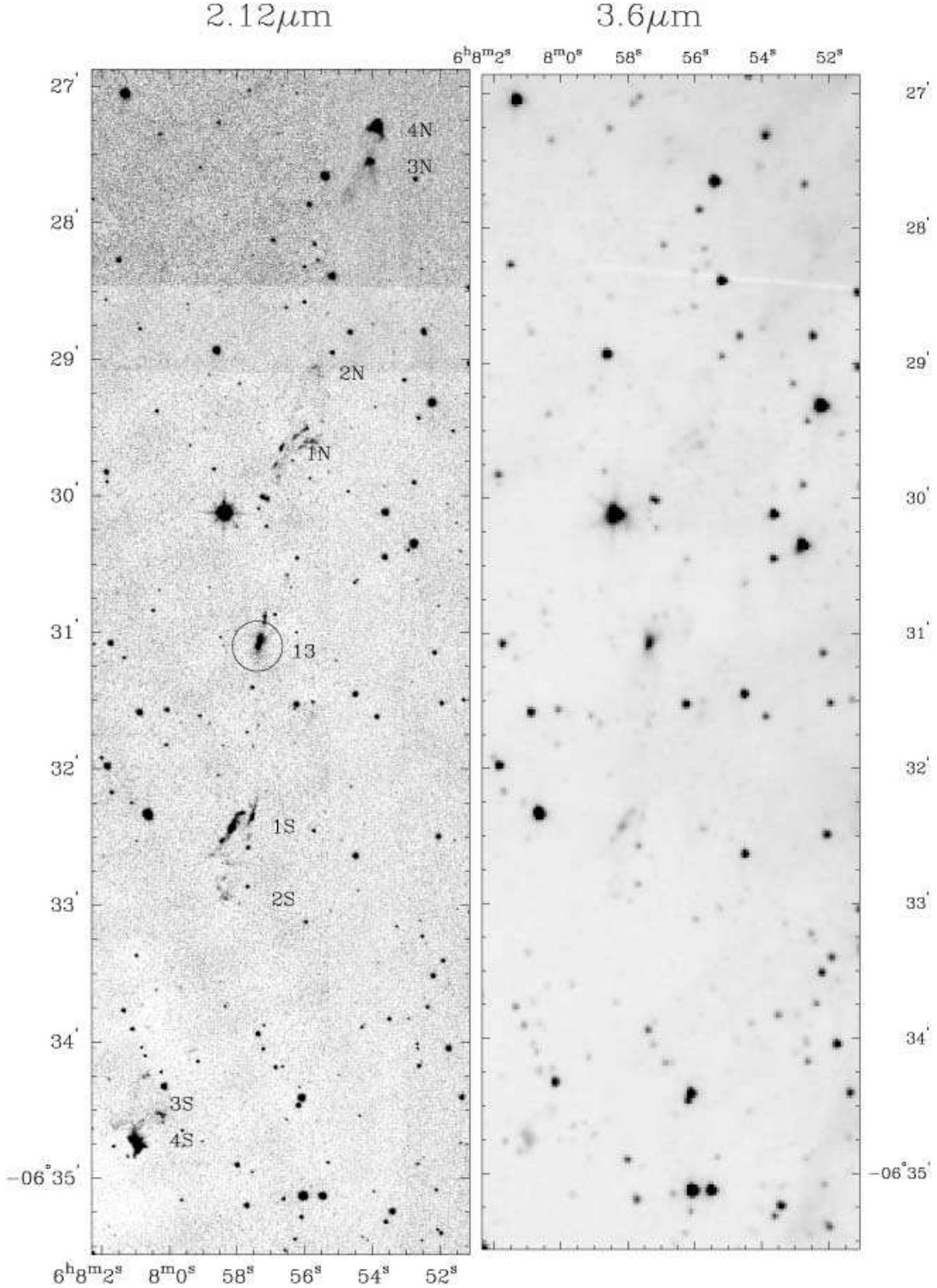


Fig. 13.— This figure shows the largest of the newly discovered jets: HOD07 13 with the central source located at  $6^{\text{h}}7^{\text{m}}57^{\text{s}}.4$ ,  $-6^{\circ}31'6''$ . The jet has a projected length of  $7.5'$ , corresponding to  $1.8$  pc. The left panel shows the UKIRT/WFCAM  $2.12 \mu\text{m}$  S(1) + continuum image, the right panel is the Spitzer/IRAC  $3.6 \mu\text{m}$  image. The area of HOD07 13 was not observed by the Spitzer/IRAC 4.5  $\mu\text{m}$  channel.

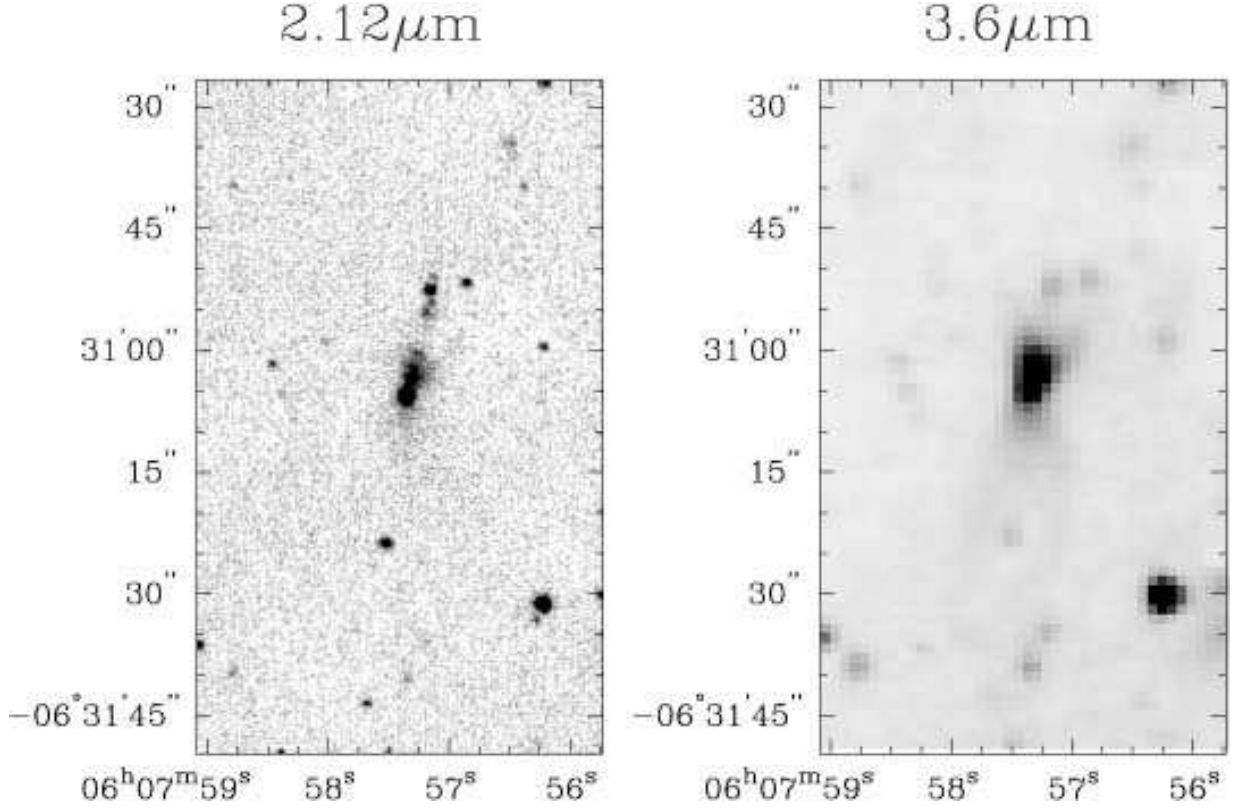


Fig. 14.— This figure shows the central region of HOD07 13. The left panel shows the UKIRT/WFCAM  $2.12\mu\text{m}$  S(1) + continuum image, the right panel is the Spitzer/IRAC  $3.6\mu\text{m}$  image. Both images show a string of shocks north of the position of the central source of this outflow. The IRAC  $3.6\mu\text{m}$  image shows emission from the southern lobe of the outflow, indicating the walls of a paraboloidal outflow cavity.

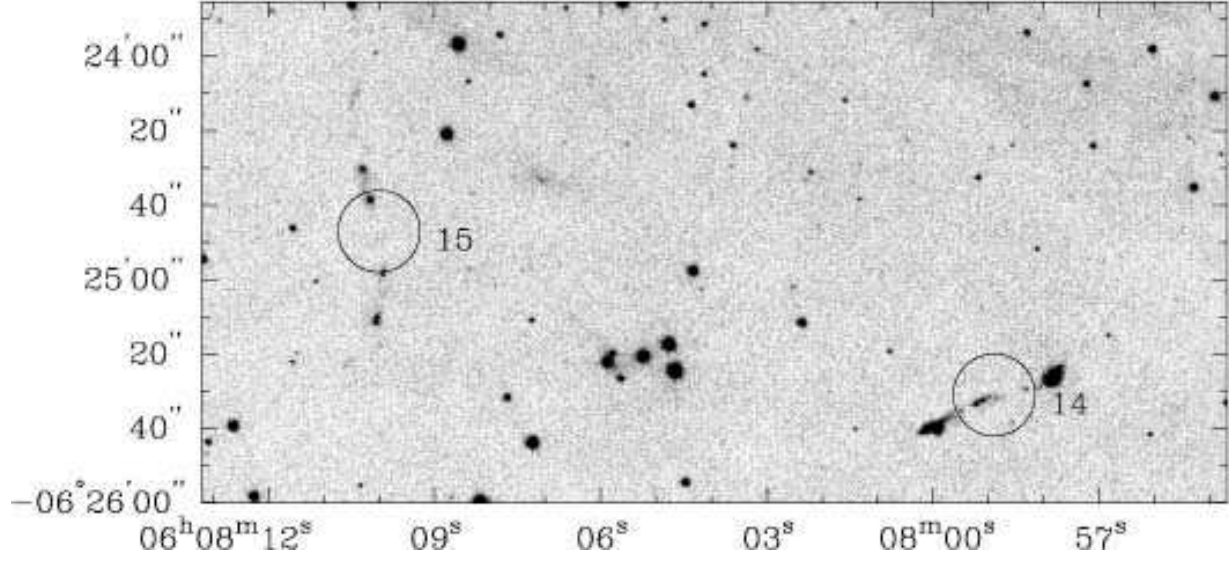


Fig. 15.— This  $2.12\ \mu\text{m}$  S(1) line + continuum image contains two separate systems of  $\text{H}_2$  knots: The likely central source of HOD07 14 is located at  $6^{\text{h}}7^{\text{m}}59^{\text{s}}.2$ ,  $-6^\circ25'33''$ . The central source of HOD07 15 is located near  $6^{\text{h}}8^{\text{m}}10^{\text{s}}.0$ ,  $-6^\circ24'47''$ .



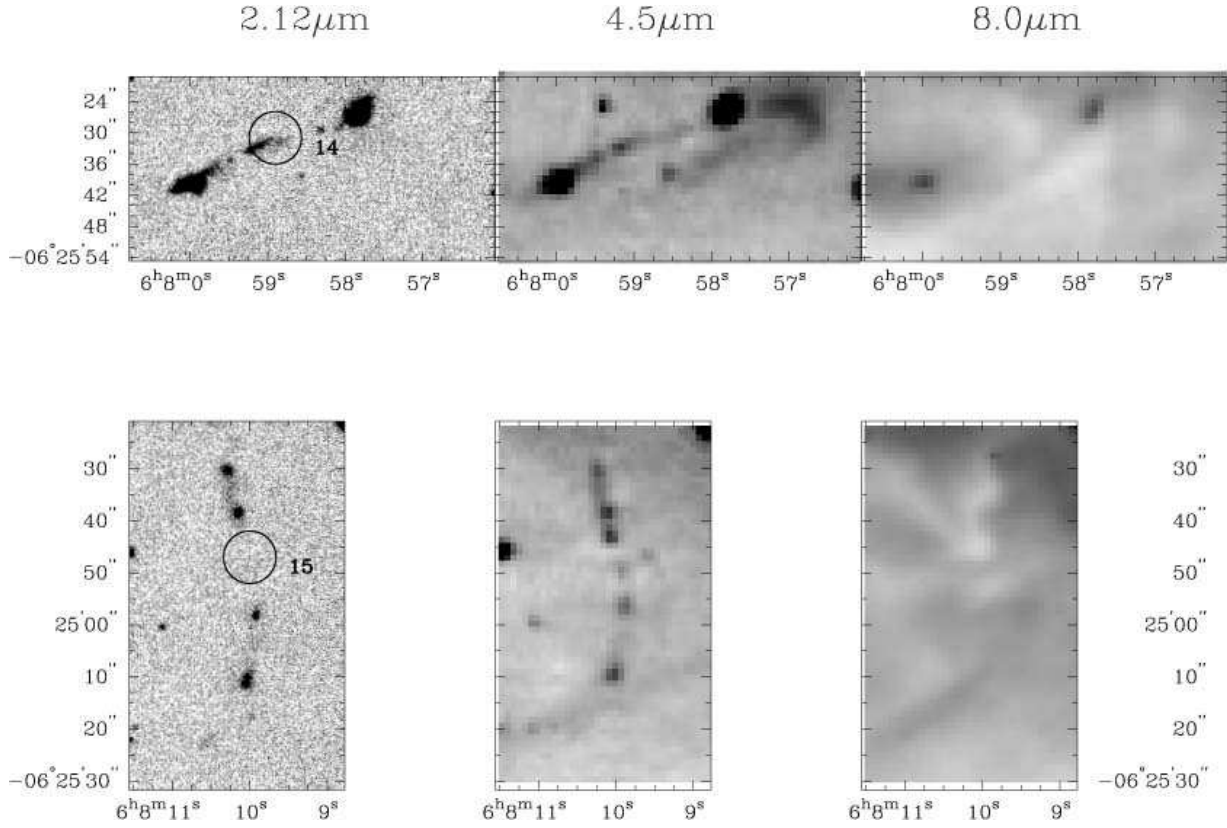


Fig. 16.— This figure contains the 2.12  $\mu\text{m}$ , Spitzer 4.5  $\mu\text{m}$ , and 8.0  $\mu\text{m}$  images of two separate systems of H<sub>2</sub> knots: The likely central source of HOD07 14 is located at 6<sup>h</sup>7<sup>m</sup>59<sup>s</sup>.2, -6°25'33". Based on the symmetry of the emission features, the central source of HOD07 15 located near 6<sup>h</sup>8<sup>m</sup>10<sup>s</sup>.0, -6°24'47".

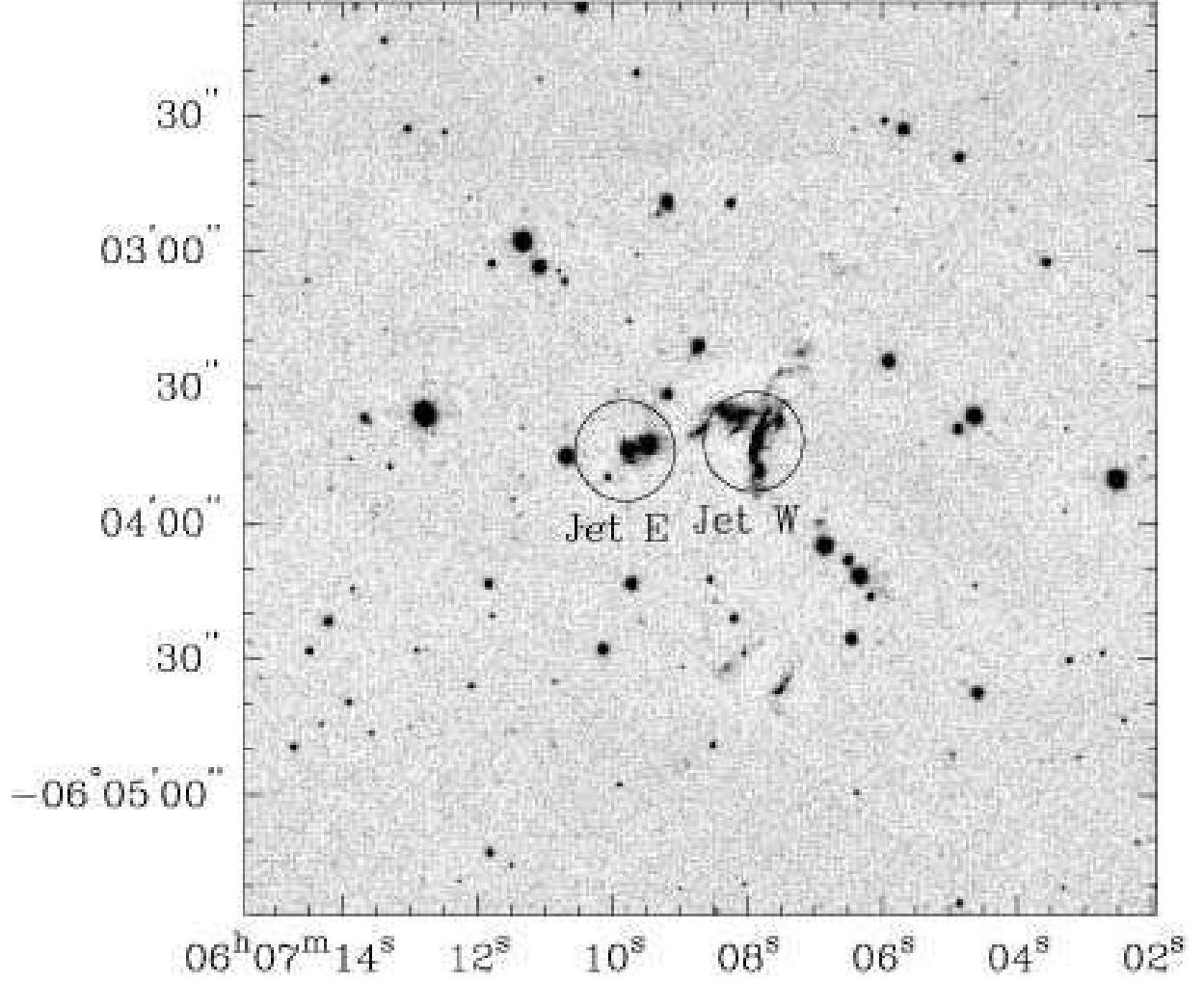


Fig. 17.— This  $2.12\ \mu\text{m}$  S(1) line + continuum image of the nebula in L 1646 associated with the optical HH object 866 (Wang, Stecklum, & Henning 2005) at  $6^{\text{h}}7^{\text{m}}7^{\text{s}}.8$ ,  $-6^{\circ}3'49''$ . We identify two  $\text{H}_2$  jets labeled Jet W and Jet E in Fig. 2 and listed in Table 1.

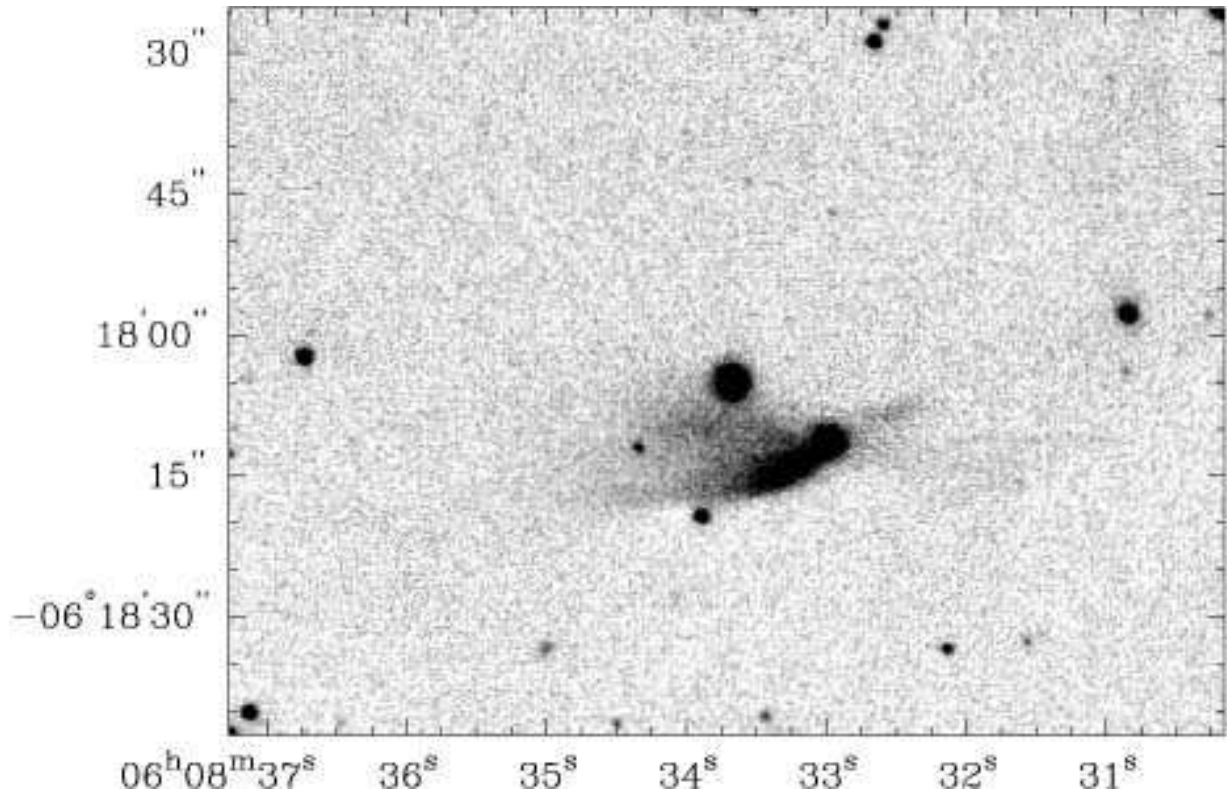


Fig. 18.— This  $2.12\ \mu\text{m}$  S(1) line + continuum image shows the bipolar reflection nebula GGD 11.

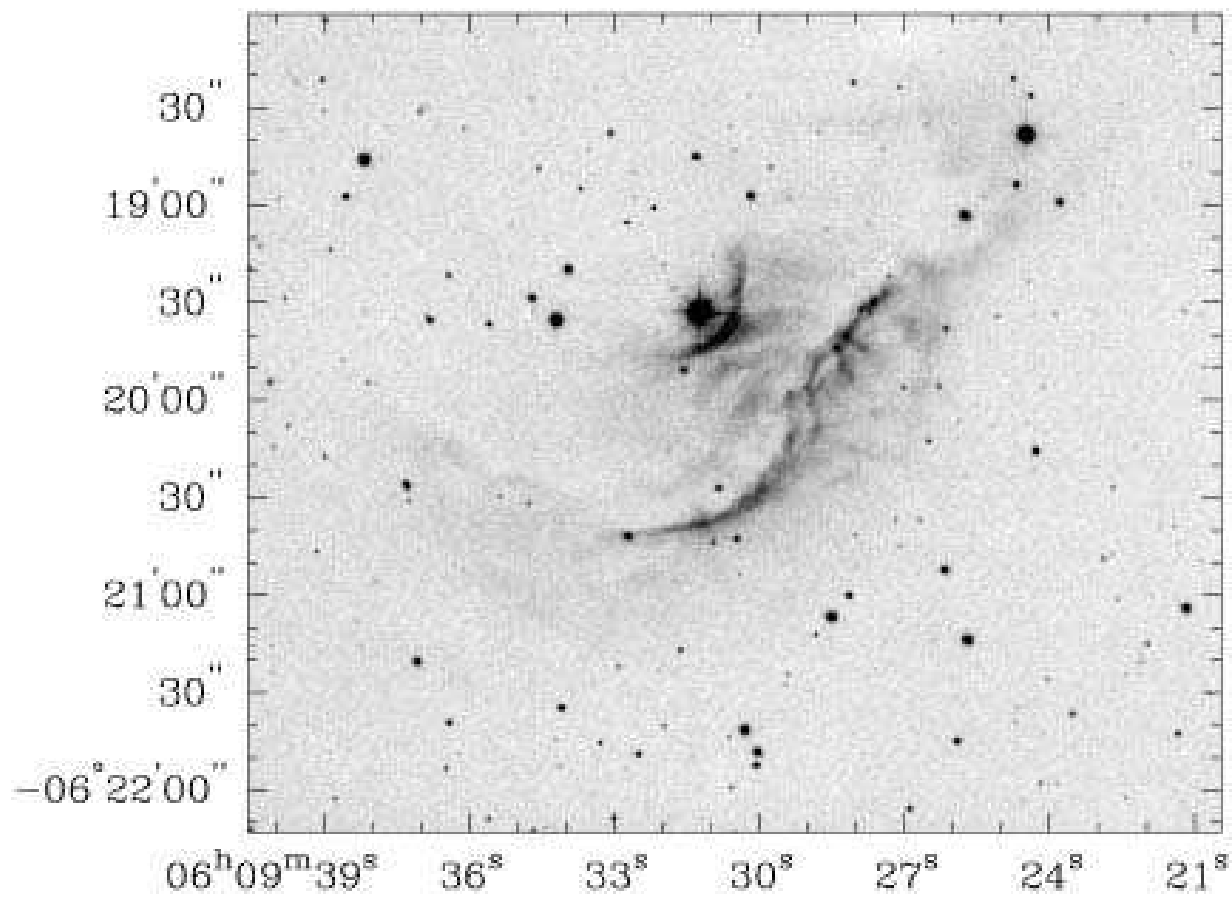


Fig. 19.— This  $2.12\ \mu\text{m}$  S(1) line + continuum image shows the reflection nebula NGC 2182, which was recorded in our large WFCAM image but not included in Fig. 1. In contrast to optical and infrared continuum images, this image shows strong, filamentary and knotty S(1) emission suggesting emission from the shock front of an expanding shell.

Table 1. Outflows in Mon R2

RA (J2000.0)	Dec (J2000.0)	Name
$6^h 7^m 07^s.9$	$-6^\circ 03' 42''$	HH 866 Jet W
$6^h 7^m 09^s.8$	$-6^\circ 03' 44''$	HH 866 Jet E
$6^h 7^m 10^s.4$	$-6^\circ 26' 34''$	HOD07 1
$6^h 7^m 30^s.5$	$-6^\circ 11' 51''$	HOD07 2
$6^h 7^m 31^s.6$	$-6^\circ 12' 47''$	HOD07 3
$6^h 7^m 37^s.6$	$-6^\circ 19' 54''$	HOD07 4
$6^h 7^m 38^s.7$	$-6^\circ 21' 14''$	HOD07 5
$6^h 7^m 39^s.2$	$-6^\circ 23' 44''$	TBWW97 CO -100,-40
$6^h 7^m 41^s.2$	$-6^\circ 11' 14''$	HOD07 6
$6^h 7^m 41^s.5$	$-6^\circ 21' 28''$	HOD07 7
$6^h 7^m 43^s.7$	$-6^\circ 10' 46''$	HOD07 8
$6^h 7^m 44^s.0$	$-6^\circ 11' 02''$	HOD07 9
$6^h 7^m 44^s.1$	$-6^\circ 23' 59''$	HOD07 10
$6^h 7^m 45^s.9$	$-6^\circ 21' 47''$	TBWW97 Mon R2-N
$6^h 7^m 46^s.8$	$-6^\circ 20' 12''$	HOD07 11
$6^h 7^m 49^s.8$	$-6^\circ 20' 43''$	HOD07 12
$6^h 7^m 57^s.4$	$-6^\circ 31' 06''$	HOD07 13
$6^h 7^m 58^s.9$	$-6^\circ 25' 31''$	HOD07 14
$6^h 8^m 10^s.0$	$-6^\circ 24' 47''$	HOD07 15

Table 2. Reflection Nebulae in Mon R2

RA (J2000.0)	Dec (J2000.0)	Name	Morphology
$6^h 7^m 11^s.0$	$-6^\circ 26' 51''$	HOD07 R1	reflection neb.
$6^h 7^m 36^s.6$	$-6^\circ 15' 07''$	HOD07 R2	bipolar neb.
$6^h 7^m 41^s.3$	$-6^\circ 20' 02''$	HOD07 R3	cometary neb.
$6^h 7^m 43^s.3$	$-6^\circ 18' 27''$	HOD07 R4	reflection neb.
$6^h 7^m 43^s.4$	$-6^\circ 11' 16''$	HOD07 R5	cometary neb.
$6^h 7^m 43^s.9$	$-6^\circ 19' 30''$	HOD07 R6	cometary neb. jet ?
$6^h 7^m 44^s.3$	$-6^\circ 25' 40''$	HOD07 R7	cometary neb.
$6^h 7^m 44^s.8$	$-6^\circ 20' 31''$	HOD07 R8	reflection neb.
$6^h 7^m 45^s.5$	$-6^\circ 25' 44''$	HOD07 R9	reflection neb.
$6^h 7^m 45^s.5$	$-6^\circ 26' 08''$	HOD07 R10	reflection neb.
$6^h 7^m 45^s.9$	$-6^\circ 25' 29''$	HOD07 R11	cometary neb.
$6^h 7^m 46^s.3$	$-6^\circ 25' 31''$	HOD07 R12	reflection nebula
$6^h 7^m 46^s.8$	$-6^\circ 25' 07''$	HOD07 R13	cometary neb.
$6^h 7^m 46^s.9$	$-6^\circ 24' 17''$	HOD07 R14	bipolar neb.
$6^h 7^m 48^s.1$	$-6^\circ 24' 05''$	HOD07 R15	reflection neb.
$6^h 7^m 48^s.2$	$-6^\circ 25' 07''$	HOD07 R16	reflection neb.
$6^h 7^m 48^s.6$	$-6^\circ 25' 22''$	HOD07 R17	bipolar neb.
$6^h 7^m 48^s.8$	$-6^\circ 25' 55''$	HOD07 R18	cometary neb.
$6^h 7^m 50^s.7$	$-6^\circ 25' 53''$	HOD07 R19	reflection neb.
$6^h 7^m 50^s.7$	$-6^\circ 26' 10''$	HOD07 R20	reflection neb.
$6^h 7^m 51^s.0$	$-6^\circ 23' 00''$	HOD07 R21	bipolar neb.
$6^h 7^m 51^s.1$	$-6^\circ 26' 10''$	HOD07 R22	reflection neb.
$6^h 7^m 51^s.3$	$-6^\circ 19' 47''$	HOD07 R23	bipolar neb.
$6^h 7^m 51^s.5$	$-6^\circ 26' 23''$	HOD07 R24	reflection neb.
$6^h 7^m 51^s.7$	$-6^\circ 23' 18''$	HOD07 R25	reflection neb.
$6^h 7^m 51^s.8$	$-6^\circ 25' 40''$	HOD07 R26	reflection neb.
$6^h 7^m 54^s.7$	$-6^\circ 26' 36''$	HOD07 R27	reflection neb.